Journal of Hazardous Materials 457 (2023) 131754

Contents lists available at ScienceDirect

Journal of Hazardous Materials

journal homepage: www.elsevier.com/locate/jhazmat

From field analysis to nanostructural investigation: A multidisciplinary approach to describe natural occurrence of asbestos in view of hazard assessment

Jasmine R. Petriglieri [a,b,c], Luca Barale [a,c], Cecilia Viti [d], Paolo Ballirano [e,m], Elena Belluso [a,b], Maria R. Bruno [f], Antonella Campopiano [g], Annapaola Cannizzaro [g], Marzia Fantauzzi [k], Flaminia Gianchiglia [e], Maria R. Montereali [i], Elisa Nardi [j], Angelo Olori [g], Fabrizio Piana [a,c], Maura Tomatis [a,h], Antonella Rossi [k], Henrik Skogby [l], Alessandro Pacella [e,*], Francesco Turci [a,c,h,**]

[a] "G. Scansetti" Interdepartmental Centre for Studies on Asbestos and Other Toxic Particulates, University of Torino, Via Pietro Giuria 9, I-10125 Torino, Italy
[b] Department of Earth Sciences, University of Torino, Via Valperga Caluso 35, I-10125 Torino, Italy
[c] Institute of Geosciences and Earth Resources, National Research Council (CNR) of Italy, Torino, Italy
[d] University of Siena, Department of Physical Sciences, Earth and Environment, Via Laterina 8, I-53100 Siena, Italy
[e] Department of Earth Sciences, Sapienza University of Rome, Piazzale Aldo Moro 5, I-00185 Rome, Italy
[f] Department of Medicine, Epidemiology, Occupational and Environmental Hygiene, National Institute for Insurance against Accidents at Work (INAIL), Lamezia Terme, Italy
[g] Department of Medicine, Epidemiology, Occupational and Environmental Hygiene, National Institute for Insurance against Accidents at Work (INAIL), via Fontana Candida 1, 00078 Monte Porzio Catone, Rome, Italy
[h] Department of Chemistry, University of Torino, Via Pietro Giuria 7, I-10125 Torino, Italy
[i] Italian National Agency for New Technologies, ENEA, Casaccia Research Centre, via Anguillarese 301, I-00123 S. Maria di Galeria, Roma, Italy
[j] Institute for Environmental Protection and Research, ISPRA, via Vitaliano Brancati 48, 00144 Roma, Italy
[k] Department of Chemical and Geological Sciences, INSTM Research Unit, University of Cagliari, I-09042 Monserrato, Cagliari, Italy
[l] Swedish Museum of Natural History, Department of Geosciences, Box 50007, SE-104 05 Stockholm, Sweden
[m] Rectoral Laboratory Fibres and Inorganic Particulate, Sapienza University of Rome, Piazzale Aldo Moro 5, I-00185 Rome, Italy

HIGHLIGHTS

- Site-specific impact of a natural occurrence of asbestos (NOA) should be assessed.
- An approach to evaluate the NOA-hazard in a natural site is presented.
- A procedure to assess if a mineral exhibits asbestos-like properties is proposed.
- A vein of asbestos-like antigorite is proved to pose a potential environmental hazard.

GRAPHICAL ABSTRACT

* Corresponding author.
** Corresponding author at: "G. Scansetti" Interdepartmental Centre for Studies on Asbestos and Other Toxic Particulates, University of Torino, Via Pietro Giuria 9, I-10125 Torino, Italy.
E-mail addresses: alessandro.pacella@uniroma1.it (A. Pacella), francesco.turci@unito.it (F. Turci).

https://doi.org/10.1016/j.jhazmat.2023.131754
Received 14 April 2023; Received in revised form 26 May 2023; Accepted 30 May 2023
Available online 1 June 2023

ARTICLE INFO

Editor: Edward Burton

Keywords:
NOA hazard
Asbestos
Elongate mineral fibre
Fibrous antigorite
Hazard assessment

ABSTRACT

The environmental impact of natural occurrences of asbestos (NOA) and asbestos-like minerals is a growing concern for environmental protection agencies. The lack of shared sampling and analytical procedures hinders effectively addressing this issue. To investigate the hazard posed by NOA, a multidisciplinary approach that encompasses geology, mineralogy, chemistry, and toxicology is proposed and demonstrated here, on a natural occurrence of antigorite from a site in Varenna Valley, Italy. Antigorite is, together with chrysotile asbestos, one of the serpentine polymorphs and its toxicological profile is still under debate. We described field and petrographic analyses required to sample a vein and to evaluate the NOA-hazard. A combination of standardized mechanical stress and automated morphometrical analyses on milled samples allowed to quantify the asbestos-like morphology. The low congruent solubility in acidic simulated body fluid, together with the toxicity-relevant surface reactivity due to iron speciation, signalled a bio-activity similar or even greater to that of chrysotile. Structural information on the genetic mechanism of antigorite asbestos-like fibres in nature were provided. Overall, the NOA site was reported to contain veins of asbestos-like antigorite and should be regarded as source of potentially toxic fibres during hazard assessment procedure.

1. Introduction

The natural occurrence of asbestos and asbestos-like minerals (NOA) poses a risk to the environment and human health when fibre dispersion occurs following natural processes and/or anthropic activities. The term "asbestos" refers to six fibrous minerals of the amphibole supergroup and serpentine group with historical or current commercial usage, due to their extraordinary physico-chemical and technological properties [1, 2]. As a result of the worldwide pandemic of asbestos-related diseases [3], the International Agency for Research on Cancer (IARC) of the World Health Organization (WHO) proved that all forms of asbestos are carcinogenic to humans [4]. Consequently, asbestos minerals were banned or strictly regulated in several countries and worldwide consumption of asbestos has generally decreased [2]. Nonetheless, the re-emergence of asbestos-related diseases was observed associated with unexpected sources and non-conventional exposure scenarios [5,6]. In addition, health and safety agencies highlighted the potential hazard posed by a plethora of "elongate mineral particles" (EMPs, NIOSH 2011 definition [7]). Some of those EMPs, e.g., fibrous glaucophane and fibrous antigorite, may share with asbestos key physico-chemical and toxicological characteristics and may pose a risk to human health [7–13]. NOA/EMP-bearing rock surfaces may be exposed to weathering and erosion and increase the environmental presence of potentially hazardous fibres [14–18]. Due to its novelty, the terminology used in the scientific community to define boundaries between asbestos, NOA, asbestos-like minerals, and fibrous minerals, largely depends on the discipline and context. To correctly address this complex semantic question, without any attempt to propose an official nomenclature, a

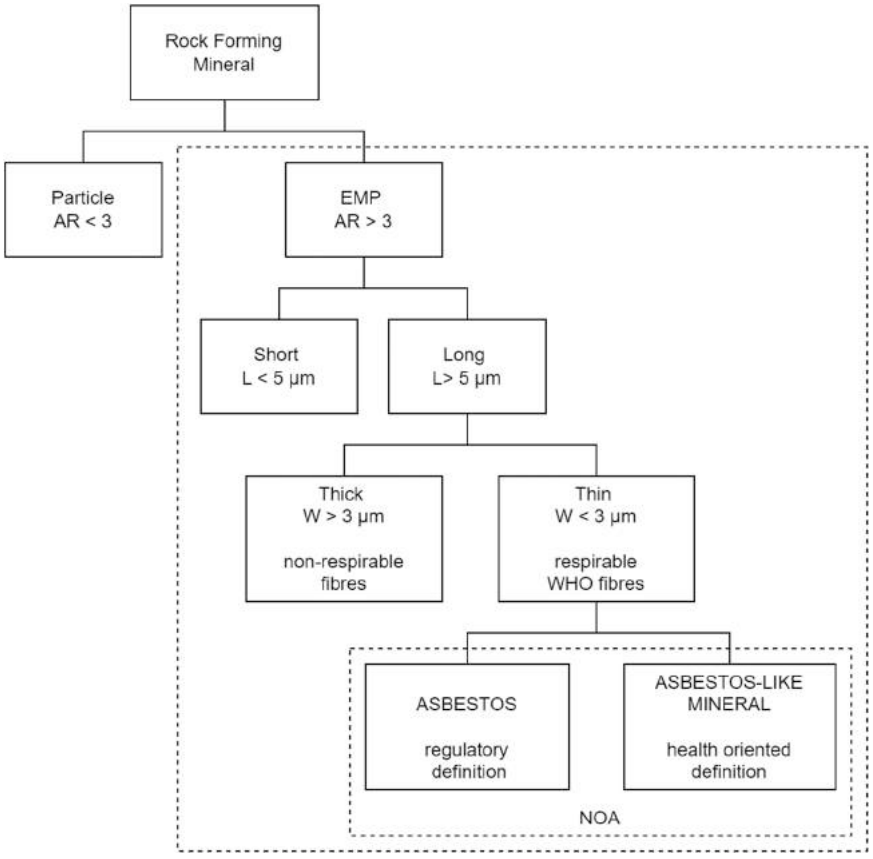

Fig. 1. Morphological definition of particles and elongated mineral particles that are investigated in this research. L, particle length; W, particle width; AR, aspect ratio = L/W. Modified after Bailey et al., 2018 [19].

morphological definition of the objects that are investigated in this research is reported in Fig. 1 and Table S1.

In this context, a multi-scale and multi-analytical integrated approach, from on-field survey to nanoscale investigation, is required to assess the hazard of a NOA fibre. The geological factors that control the growth of NOA fibres in a site-specific natural setting are pivotal in: i) quantifying the occurrence and distribution of NOA; ii) understanding the mechanism of formation of respirable NOA fibres; and iii) developing methodological and analytical procedures to evaluate the NOA hazard. An integrated hazard assessment based on structural-geological field evidence combined with textural, mineralogical, and petrological investigations is the first step in the evaluation of NOA hazard [20]. A close relationship between the occurrence of NOA and the rock fabrics, which is in turn derived from the combined activity of deformation, metamorphism/metasomatism, and fluid/rock interaction, was indeed recently investigated (e.g., [21,22]).

The pathogenic potential of an inhalable poorly soluble mineral particle depends on three main morpho-chemical aspects, i.e., the particle morphology, its crystal-chemistry, and the consequent mineral alteration, which modulates the surface reactivity upon particle inhalation [23]. The scientific community agrees that i) the size and shape, ii) the biopersistence, and iii) the surface reactivity of a fibre are the key modulators of lung toxicity [4]. Therefore, in the definition of the toxicological profile of a suspected NOA, structural and physico-chemical properties, including morphology, chemical composition, biodurability/biopersistence, and surface reactivity need to be evaluated ([24] and therein).

Fibre morphology affects deposition, translocation, and clearance of the fibre to, in, and from the lung, ultimately defining the fibre fate in the human body [25]. Asbestos fibres exhibit a distinct morphology, consisting of bundles of very long and thin, elongate particles with a poly-filamentous behaviour [4]. Asbestos fibres easily split along the growth c-axis, resulting in long and thin fibres even after strong mechanical stress ([26] and therein). Wylie and co-workers [27] highlighted how the aerodynamics of fibres in the respiratory system is governed mostly by size parameters, notably by the fibre width [27–29]. Long and thin fibres are suspected to be more potent than short and thick fibres in the induction of asbestos-related diseases [4,30]. From a regulatory and morphometric point of view, this led WHO to define a *respirable fibre* of asbestos as a particle with length L $>$ 5 μm, width W $<$ 3 μm, and length to width ratio (aspect ratio, AR=L/W) $>$ 3 [1]. In 2011, NIOSH introduced EMP and expanded the dimensional boundaries of "asbestos fibre" to all the potentially hazardous elongate mineral particles with AR $>$ 3 and length $>$ 5 μm, as determined by phase-contrast microscopy (PCM) [7]. However, in the complex realm of NOA, a plethora of different morphologies may be observed, and further differentiation might be determined by the scale of observation. Elongate minerals may exhibit habits that span from platy-lamellar to fibrous asbestos-like, including all the intermediate "pseudo-fibrous" forms (e.g., [31]) when observed at the macroscopic scale. As a result, a suspected NOA must exhibit an asbestos-like morphology at the microscopic scale and this parameter must be quantitatively assessed.

Although the correlation between asbestos-like habit and pathogenicity is universally accepted [4], elongate morphology does not imply toxicity per se. Structural and chemical properties define the solubility of fibres [32–35], playing an important role in bio-durability [36]. The toxicologically-relevant dissolution rate of a mineral fibre is often inferred with simulated body fluids (SBF) to gain insight on the residence time of a fibre at the site of deposition. The longer a fibre resists chemical alteration, the greater is the probability that adverse interaction between fibre and biological media occurs [37]. Several durability tests in dynamic and static fluids have been recently proposed to assess the congruent vs. incongruent chemical dissolution of fibres [38,39].

Mineral toxicity also involves reactions that take place at the bio-inorganic interface, including dissolution/reprecipitation reactions that either regulate the surface chemistry or segregate ions in neo-formed nanoscale mineral phases. It must be also considered the possibility of a mineral surface to chemically modify biomolecules via redox reactions. Mechanism-based structure-activity relationship for asbestos includes generation of reactive oxygen species (ROS; [40,41]). Primary, fibre-induced, ROS production at fibre surfaces is mediated by transition metal ions, specifically iron [24,42], and is responsible for chronic inflammation, together with cell-derived ROS [43,44]. The role of iron chemical state is here investigated and the possible correlation between ROS production and presence of iron (II) on the fibre surfaces discussed [41].

This work aims to define a multianalytical protocol for evaluating whether a fibrous mineral occurring in a specific NOA site might represent an environmental and health hazard. Specifically, the approach describes from field analysis to nanostructural investigation, the pathway to support the identification of an asbestos-like mineral from a natural outcrop. The feasibility of this approach is demonstrated here: a sample of fibrous antigorite from a specific NOA site in Varenna Valley NOA (Liguria, Italy) was selected and investigated to determine the key physico-chemical parameters that may confer hazardous properties to a mineral. The lack of a well-defined toxicological profile makes fibrous antigorite a good candidate for the investigation of asbestos-like properties, in view of its toxicological assessment ([13] and therein). In this work, the asbestos-like morphology, the crystal-chemical structure and the mineral dissolution, together with the toxicity-relevant surface properties of a selected fibrous antigorite specimen were investigated. We shed light on the genetic mechanism by which crystal growth forms asbestos-like fibre, on how lattice and surface chemistry regulate dissolution in simulated fluids and redox reactivity. Overall, this work presents new evidence on the potential hazard of fibrous asbestos-like antigorite and describes a general approach for investigating potentially asbestos-like minerals in natural sites.

2. Materials and methods

2.1. Samples

Potentially fibrous antigorite was collected from one vein (VV3) among several veins from a NOA site (see Results par. 3.1) in Varenna Valley (Genoa, NW Italy). UICC (Union for International Cancer Control) standard asbestos crocidolite ($Na_2Fe_2^{3+}(Fe^{2+},Mg^{2+})_3Si_8O_{22}(OH)_2$, specific surface area (SSA, N_2-BET method = 8 m^2/g, [45]), and chrysotile A (from Zimbabwe, $Mg_3Si_2O_5(OH)_4$, SSA = 27 m^2/g, [46]) were used to comparatively investigate antigorite properties. Specifically, crocidolite was used to define antigorite fibrous morphology (FPIA analysis and SEM, see Par. 3.3) and chrysotile to estimate durability and surface reactivity of antigorite (see Par. 3.6 and 3.7).

2.2. Sample preparation

Vein samples were collected by hand-picking with stainless steel tweezers after gently removing the superficial portion of the potentially weathered material with the pointed tip of a pick hammer. Vein antigorite fragments were preliminary gently crushed and sieved to obtain a fraction $<$ 2 mm. This fraction was ground following two different protocols: i) for the morphological evaluations and ii) for the dissolution and surface reactivity tests.

Sample preparation i): the $<$ 2 mm fraction (1.8 g) was dry ground in a ball mixer mill (Retsch MM200) for 2, 5, 10, and 20 min at 27 Hz using an agate jar (15 ml) with 4 agate balls (5 mm diameter). Agate jars were used to avoid metal contamination. After grinding, powder samples were sieved at 300 μm.

Sample preparation ii): the $<$ 2 mm fraction (5.5 g) was wet ground in a planetary ball mill (Fritsch P6) for 5 min at 450 rpm using a zirconium oxide jar (45 ml) with 4 g of zirconium oxide balls (5 mm diameter). Zirconium oxide jar was used to avoid metal contamination. After grinding, powder samples were washed in ultrapure water by

centrifugation (8000 rpm for 20 min), sieved at 100 μm, and dried at low temperature (60 °C).

2.3. Bulk and surface characterization

2.3.1. X-ray powder diffraction (XRPD)

XRPD analysis of the antigorite sample was performed using a Bruker AXS D8 Advance (Bruker AXS, Karlsruhe, Germany) operating in θ/θ transmission mode. The powdered sample was prepared as capillary. The instrument is fitted with incident-beam focusing Göbel mirrors and a PSD Våntec-1. Data were collected at 40 kV and 40 mA, using CuKα radiation in the 5–145°2θ angular range, 0.0218°2θ step-size, and 10 s of counting time.

2.3.2. Micro-Raman spectroscopy

Raman spectra were obtained with a Horiba HR800 Raman spectrometer equipped with an Olympus BX41 confocal microscope, a 600-grooves/mm holographic grating monochromator, and a high-gain Peltier-cooled CCD. A Nd solid state laser at 532-nm was used as excitation and neutral density filters were used to avoid sample heating. Spectra were obtained on vein fragments and polished thin sections (30 μm thick) with a 10x and 100 × objective, respectively. Under these working conditions, the minimum lateral resolution is around 2 μm and the resolution along the z-axis is about 1 μm with 100x objective. The spectrometer was calibrated using the 520.7 cm^{-1} Raman peak of silicon before each experimental session. Spectra were collected as follows: 6 acquisitions for 20 s in the low and high wavenumber spectral range were averaged and background subtracted with LabSpec® software.

2.3.3. Scanning and transmission electron microscopies

Secondary Electron Images (SEI) were acquired at various magnifications using a Scanning Electron Microscope (SEM) ZEISS EVO50 XVP equipped with an X-Stream OXFORD EDS (accelerating voltages, commonly 3–10 kV).

Transmission Electron Microscopy (TEM) analyses were performed by a JEOL 2010 microscope, working at 200 kV, LaB_6 source and ultra-high resolution (UHR) pole piece, allowing point-to-point resolution of 0.19 nm. The microscope is equipped with semi-STEM control and ultra-thin window energy dispersive spectrometer (EDS ISIS Oxford). Data was recorded by an Olympus Tengra CCD camera. Antigorite powder (see comminution, Par 2.2ii) was deposited on mesh Cu grids with supporting lacey carbon films. We also prepared ion-milled samples extracted from petrographic thin sections (perpendicular to vein direction), using Gatan DuoMill and PIPS ion milling systems.

2.3.4. Electron microprobe analysis (EMPA)

The chemical composition of the antigorite fibres was determined using a Cameca SX-50 electron microprobe equipped with five wavelength-dispersive spectrometers (WDS) using the following conditions: accelerating voltage 15 kV, specimen current 15 nA, beam diameter 10 μm, 20 count time (peak), 10 count time (background). The following standards were used: wollastonite (Si Kα, Ca Kα), rutile (Ti Kα), corundum (Al Kα), magnetite (Fe Kα), metallic Mn (Mn Kα), periclase (Mg Kα), orthoclase (K Kα), jadeite (Na Kα), metallic Cr (Cr Kα), fluorophlogopite (F Kα), and sylvite (Cl Kα). Antigorite sample was prepared for electron microprobe analysis by embedding the fibres in epoxy resin.

2.3.5. Mössbauer spectroscopy

Mössbauer spectra were acquired using a conventional spectrometer system operated in constant-acceleration mode. The Mössbauer absorber was prepared by mixing 50 mg of powdered antigorite (see comminution, Par 2.2ii) with about 100 mg acrylic resin. The mixture was pressed to a 12 mm diameter disc under mild heating. The spectrum was collected at room temperature using a standard ^{57}Co source in a Rh matrix with a nominal activity of 50 mCi and the absorber placed in 54.7° to the incident beam to avoid texture effects. Spectral acquisition was obtained over 1024 channels in the velocity range − 4.5 to + 4.5 mm/s, and the data was then calibrated against a spectrum of an α-Fe foil before folding and fitting using the software MossA [47]. The spectrum was fitted with one quadrupole doublet assigned to Fe^{3+} and two doublets assigned to Fe^{2+}, applying Lorentzian line shapes and equal intensities of the quadrupole components.

2.3.6. Flow particle image analysis (FPIA)

Particle shape and particle size distribution of comminuted antigorite (see comminution, Par 2.2i) in a range of 0.8–300 μm were obtained by FlowParticle Image Analysis (FPIA) using the Sysmex FPIA-3000 apparatus (Malvern Instruments). Antigorite powders were dispersed in ultrapure water (0.5 mg/ml) and sonicated for 30 s at 10 W. Each suspension was passed through a cell where images of particles were captured using stroboscopic illumination and a CCD camera (20 × magnification lens). More than 2000 particles were analysed for each specimen.

2.3.7. Specific surface area (SSA)

Specific surface area was determined by Kr adsorption at 77 K, using an automatic gas-volumetric apparatus (ASAP 2020, Micromeritics, USA), and adopting the well-known BET method [48]. SSA of comminuted antigorite prepared for dissolution and surface reactivity tests (see comminution, Par 2.2ii) is 5.7 m^2/g.

2.4. Durability in simulated body fluids

2.4.1. Dissolution test

The dissolution of antigorite was studied under static leaching conditions. The leaching solution was prepared using ultrapure deionized water (18.2 MΩ cm at 25 °C) obtained from a MilliQ Element system (Millipore) and the following reagents and materials: NaCl RPE-ACS (Carlo Erba Reagents, DASIT Group, Milan, Italy), $Na_2SO_4 \times 10\ H_2O$ (Carlo Erba Reagents, DASIT Group, Milan, Italy), and $Na_3C_6H_5O_7 \times 2\ H_2O$ RPE (Carlo Erba Reagents, DASIT Group, Milan, Italy); Polypropylene Falcon Tubes (BD FalconTM, Corning, Mexico) were used during samples handling, syringes (BD PlastipackTM, Spain) and 0.22 μm GSWP nitrocellulose membrane filters (Millex-HA, Millipore, Ireland) were adopted for samples filtration. The pH measurements were performed using a portable 250 A Orion pH Instrument (Orion Research Inc., Boston, USA) equipped with an Orion gel-filled combination semi-microelectrode (Thermo Electron Corp., Cambridge, England). Dissolution experiments were carried out in a mimicked Gamble solution (MGS) according to Rozalen et al. (2013): NaCl 112.3 mM and $Na_2SO_4 \times 10\ H_2O$ 556 $mmolL^{-1}$, with the addition of $Na_3C_6H_5O_7 \times 2\ H_2O$ 0.150 mM (i.e., that typical of lung fluids) as a chelating agent. The solution pH was adjusted to the starting value of 4.5 with HCl. Notably, although far from mimicking the complexity of a cellular system, such experimental conditions were chosen to promote the dissolution dynamics that may occur in vivo, in a reasonable experimental time, during the interaction between fibres and lysosomal fluid of alveolar macrophages.

An amount of 20 mg of powder sample (see comminution, Par 2.2ii) was suspended in 40 ml of MGS, placed in a Falcon™ polypropylene tube, at 37 ± 1 °C. Continuous waving was provided by a thermostatted oscillating vessel. Experiments were performed in quadruplicate for 1 h, 24 h, and 168 h (1 week), and the following procedure was carried out for each set of experiments. At established time points, the fibres were separated from the solution by filtration through a nitrocellulose membrane of porosity 0.22 μm, and the amount of magnesium, silicon, iron and aluminium in the supernatant was measured by Inductively coupled plasma optical emission spectroscopy (ICP-OES).

2.4.2. Inductively coupled plasma optical emission spectroscopy (ICP-OES)

The analysis of the solutions following the leaching tests was

performed by ICP-OES for determining the concentration of the dissolved ions and whether the dissolution is congruent or not. All measurements were performed using a Perkin–Elmer Optima 2000 DV ICP-OES spectrometer (Perkin-Elmer, Norwalk, CT, USA) equipped with a cyclonic spray chamber. ICP Aristar (BDH) standard solutions in nitric acid for the investigated elements were used to prepare the calibrating solutions for ICP-OES analysis. 1 ml of each filtered solution was diluted 1:20 with a 1% nitric acid solution. Data reported are the mean values of quadruplicate measurements (corrected for the blank).

2.4.3. X-ray photoelectron spectroscopy (XPS)

X-ray photoelectron spectroscopy (XPS) is a powerful tool for the investigation of mineral surface exposed to both biotic and abiotic environments. [49] In this work XPS data allow obtaining the elemental and quantitative composition of the surface of the antigorite sample before and after the contact with solutions, which simulate the chemical environment in biological fluids. Furthermore, XPS provides the chemical state of iron at the surface of the fibrous minerals, that is known to be related to the mineral toxicity. To prevent oxidation, samples were stored in a glovebox under argon prior to XPS analysis. XPS analyses were performed using a Theta Probe spectrometer manufactured by Thermo Fisher Scientific (East Grinstead, UK) equipped with a monochromatic Al kα X-ray source (100 Watts). The spectra were acquired in the standard lens mode using a 400 μm nominal spot-size; the analyser was operated in the fixed analyser transmission mode and the pass energy was set at 200 eV and 100 eV for survey and high-resolution spectra, respectively. The base pressure during the analysis was about 10^{-7} Pa. The vacuum system includes rotary pumps, turbomolecular pumps and a titanium sublimation pump. The emission angle was 53 degrees in respect to the perpendicular to the sample surface. In order to compensate for sample charging, a combined low energy electron/Ar ion flood gun was used as neutralizer, and the binding energy values were referred to the adventitious aliphatic carbon at 285.0 eV. Pristine samples were analysed as powders deposited on Indium foil. Samples incubated for 1 week in the MGS solution were analysed as powder deposited on nitrocellulose membrane filters. Further details on the spectrometer calibration, linearity of the binding energy check according to ISO 15472:2010, spectra acquisition conditions and quantification are provided in Fantauzzi et al. [50,51]. Data processing was performed using CasaXPS software.

2.5. Surface reactivity in free radical release

Surface reactivity in hydroxyl and carboxyl radical generation was evaluated by spin trapping technique associated with Electron Paramagnetic Resonance (EPR) on Miniscope 100 EPR spectrometer (Magnettech, Berlin, Germany). Instrument settings were as follows: microwave power, 10 mW; modulation, 1 G; scan range, 120 G; centre of field 3330 G, gain $9{\cdot}10^2$. 5,5-dimethylpirroline-N-oxide (DMPO; Cayman Chemical Company) was used as a spin trap. The tests were performed at 37 °C in absence of light and the EPR spectra were recorded on 50 μl of suspension after 10, 30, and 60 min of incubation with the target molecules. The amount of radical released is proportional to the intensity of the EPR signal. The experiments were performed at least in duplicate, and a blank procedure was carried out. The following protocols were employed:

2.5.1. Hydroxyl radical generation

0.2 m^2 of sample were suspended in 500 μl of 0.5 M potassium phosphate buffer (pH 7.4) and 250 μl of DMPO (0.18 M). The reaction was triggered adding 250 μl of H_2O_2 (0.2 M).

2.5.2. Carboxyl radical generation

0.2 m^2 of sample were suspended in 250 μl of DMPO (0.18 M) and 250 μl of ultrapure MilliQ water. The reaction was started adding 500 μl of sodium formate (2 M) in 1 M phosphate buffer (pH 7.4). The experiments were repeated in a reducing environment by adding 250 μl ascorbic acid (3 mM) instead of the ultrapure water.

3. Results and discussion

3.1. Geological assessment and sampling strategy

The sampling site is located in the Varenna Valley near the city of Genoa (NW Italy), in the '*interference zone*' (*sensu* [52]) between Western Alps and Northern Apennine orogenic chains. The site belongs to the Palmaro–Caffarella tectono-metamorphic Unit, lying in the south-easternmost part of the Voltri ophiolite 'massif', at the contact with the large tectonic slice zone known as Sestri–Voltaggio Zone ([53, 54]; Fig. 2a, b). The Voltri 'massif' is one of the main meta-ophiolite units of the Western Alps, derived from the metamorphism of portions of mantle and oceanic crust (including the overlying Jurassic-Cretaceous sedimentary cover) ascribed to the Liguria-Piemonte Oceanic Domain (e.g., [54–57]).

The Palmaro–Caffarella tectono-metamorphic Unit includes meta-ophiolites and related meta-sedimentary cover which underwent a metamorphic evolution with blueschist-facies peak conditions and a more or less developed greenschist-facies overprint [54,58]. The meta-ophiolites of the Palmaro–Caffarella Unit mainly consist of antigorite serpentinite (*Serpentiniti di San Carlo di Cese* unit), with hectometre-sized bodies of meta-gabbro and meta-basite. The meta-sedimentary cover is represented by a thin layer of quartz-schist, followed by a marble and calcschist succession (*Calcescisti della Val Branega* unit) [53].

The area surrounding the sampling site (Fig. 2c, d) was mapped at the 1:5000 scale by the authors during a geo-environmental study in the context of the *Gronda di Genova* tunnel system project (see [59]).

The sampling outcrop (coordinates: 44°27'22.2"N; 8°49'08.9"E) is located in the Varenna streambed, on the left side of the stream, between Carpenara and Chiesino localities (Fig. 2d). This part of the Palmaro–Caffarella tectono-metamorphic Unit is characterised by a complex lithological alternation at the decametre- to hectometre-scale (Fig. 2c). The lithological alternation results from folding and shearing of different lithotypes, including serpentinite, metabasite, chlorite-actinolite schist, calcschist and marble, whose distribution is controlled by tight folds (locally isoclinalic) with a decametre to metre wavelength and ENE–WSW-directed axes. This complex geometric setting was further complicated by the activity of faults and shear zones, which affected the rock volume after folding and generated fault breccias and cataclasites. When the geological mapping was carried out (years 2007–2010), the described faults and shear zones were well exposed on the front of the inactive quarry located on the right side of the Varenna Stream south of the sampling outcrop (Fig. 2c). The quarry has later become a spoil dump and the quarry front is presently largely masked by spoil piles.

The sampling outcrop consists of a decametre-sized antigorite serpentinite body (Fig. 3.a). The contact with the embedding calcschist is marked by a dm-thick layer of foliated breccia composed of sub-rounded clasts of both veined serpentinite (ophicalcite) and calcschist, in a carbonate matrix. The serpentinite is generally non-foliated and crossed by cm-thick and several-metres-long antigorite veins (Fig. 3.b).

At the mesoscale, the antigorite veins exhibit a pale green to whitish colour and a splintery aspect, deriving from a more or less evident tendency to fragment into mm-large and mm- to cm-long, straight to slightly curvilinear fragments (Fig. 3.c). The antigorite vein (Fig. 3.a, b) was selected for its markedly fibrous aspect. This vein has an ENE–WSW direction (mean orientation: 318/78) and an aperture varying from a few to 20 mm and can be followed for several metres on the outcrop surface. The orientation of the mineral fibres within the vein and the geometry of the vein walls indicate that it is a sinistral shear vein. The antigorite fibres grow parallel to the shear direction and thus generally parallel to the vein walls (slip fibres), except in dilational jogs. These are

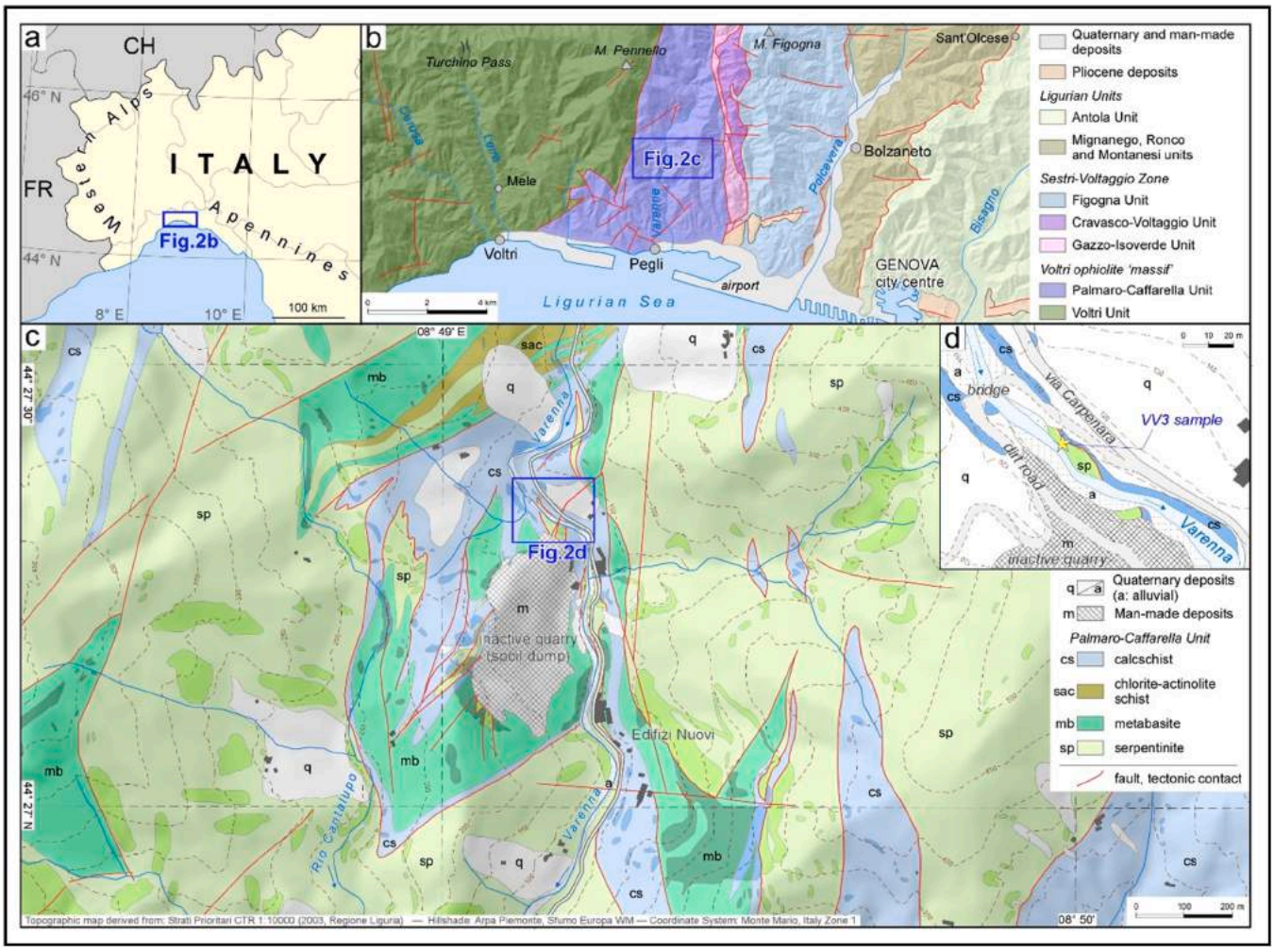

Fig. 2. a) Position of the studied area. b) Tectonic scheme of the Genoa area, after Capponi and Crispini, 2008 [53]. c) Geological map of the middle Varenna Valley, based on unpublished authors' surveys at the 1:5000 scale (years 2007–2010); darker hues correspond to outcrops. d) Detail outcrop map showing the position of the selected antigorite vein outcrop. Same legend as c).

vein portions with walls forming a high angle with respect to shear direction; in these sites, fibres thus grow at a high angle with respect to the vein walls (cross fibres; Fig. 3.b).

Under the optical microscope, antigorite appears colourless to pale green/yellow and shows a low birefringence (Fig. 3d,e and Supplementary Materials S2). The vein is formed by elongate to fibrous antigorite crystals, broadly sharing the same elongation axes, parallel to shear direction (Fig. 3d). Cross-section observations reveal that antigorite elongated crystals display rotational disorder around their elongation axis, as highlighted by (001) orientation in Fig. 3e.

3.2. Collection, separation, and preliminary characterization of antigorite

A preliminary mineralogical identification and morphological assessment was performed on a potentially asbestos-like antigorite vein sampled to minimize the presence of accessory minerals.

XRPD analyses confirmed the occurrence of antigorite in the investigated vein. Micro-Raman spectroscopy was performed on vein fragments. The presence of the typical doublet in the OH stretching region, with the main peaks located at about 3668 and 3697 cm^{-1}, allowed us to confidently assign antigorite (Fig. 4a; [60–63]). More than 50 Raman spectra were collected from different specimen portions and all of them were assigned to antigorite, thus indicating that antigorite is the predominant serpentine phase in the selected specimen. Fig. 4b shows a representative SEM image of an elongated antigorite fibre, which consisted of poly-filamentous bundles of tightly packed fibres and fibro-lamellae. Bundles of parallel elongated lath-shaped crystals may present regular or irregular endings.

3.3. Evaluation of the asbestos-like morphology

Antigorite is a common rock-forming metamorphic mineral, being the main constituent of antigorite serpentinites where it typically grows with a platy-lamellar habit (e.g., [64–67]). When grown in veins, antigorite may occur with different morphologies, from platy-lamellar to fibrous asbestos-like (e.g., New Caledonian antigorite [68–70]), including all intermediate "pseudo-fibrous" forms (e.g., [71–74]).

To verify whether selected antigorite from Varenna Valley exhibits an asbestos-like morphology, we performed a morphometric characterization of the samples that were subjected to a standardised mechanical stress at several time points (2, 5, 10, 20 min of comminution - see Par. 2.2.i). The choice of the standardized mechanical stress used for the evaluation of asbestos-like morphology was of pivotal importance and stemmed out from previous works on the lingering question between asbestos vs. non-asbestos like elongated minerals [75–77]. Mid-to-long term milling procedures performed on non-asbestos-like minerals are expected to modify the size distribution, the shape, and the crystallinity of fibres [75]. In particular, the prevalent reduction of the lengths of elongated crystals with respect to their diameters is expected. In these cases, macroscopically elongated minerals tend to

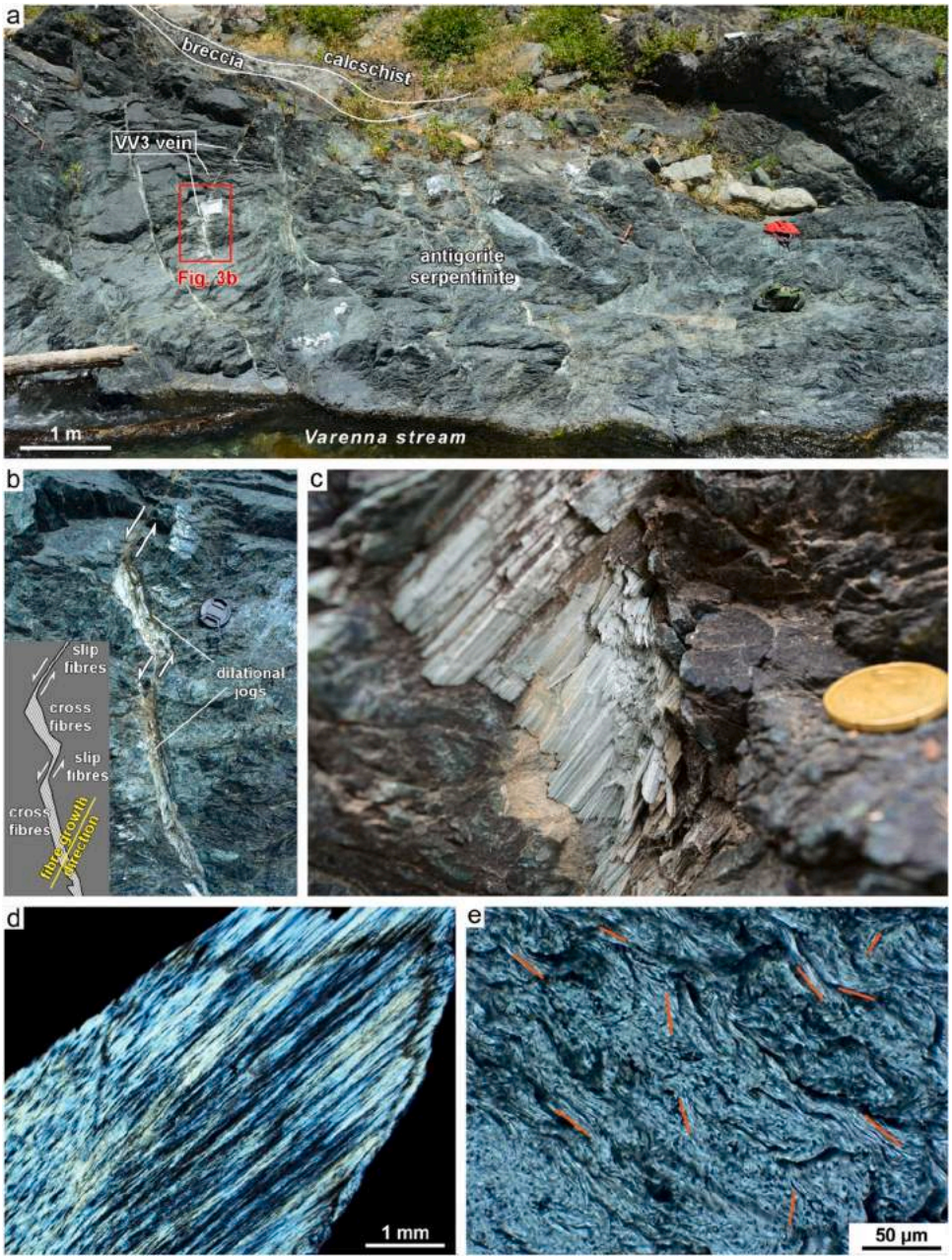

Fig. 3. Meso- and micro-scale features of antigorite vein (Atg) and its host rock. a) Part of the decametre-sized antigorite serpentinite body hosting the Atg vein, cropping out along the Varenna stream. The contact with the embedding calcschist is visible in the upper part of the image and is marked by a dm-thick breccia layer. The serpentinite is cut by several antigorite veins visible as thin, light green bands; b) Image and sketch of a portion of fibrous antigorite vein. The arrow pairs indicate the sense of shear. Fibres grow parallel to the shear direction, forming slip fibres in the vein portions with walls parallel to the shear direction and cross fibres in dilational jogs (i.e., vein portions with walls forming a high angle with respect to shear direction). Lens cap for scale is 52 mm in diameter; c) Detail of a dilational jog of Atg vein, with cm-long cross antigorite fibres. Coin for scale is 22 mm in diameter; d) Thin section photomicrograph (cross-polarized light) of Atg vein cut parallel to the fibre elongation and showing the characteristic "fibrous" texture of antigorite; and e) Thin section photomicrograph (cross-polarized light) of Atg vein cut perpendicular to the fibre elongation. The orange lines highlight the orientation of (001) cleavage planes of antigorite crystals, observed in their *ac* sections and randomly oriented around [010] (i.e., shear direction).

generate isometric particles when milled (i.e., particles with AR <3; [78]). Conversely, asbestos and asbestos-like mineral fibres preserve their typical fibrous morphology during mid-to-long term comminution [77], because they preferentially split along the elongation growth axes of the crystal. Under such circumstances, the milled fibres will still meet the dimensional criteria that are assumed to be relevant for hazardous fibrous minerals (e.g., [1]). The milling procedure designed in this study allowed us to estimate the variation of the morphometric parameters, i.e., the % of particles, EMP, WHO fibres, and non-respirable fibres (Fig. 1 and Table S1) and describe the asbestos-like morphological behaviour of the investigated antigorite specimen. In general, we believe that this approach can be used to quali-quantitatively solve the lingering discrimination between asbestos and non-asbestos-like behaviour of macroscopically elongated, potentially hazardous NOA.

Morphometric parameters were obtained for each comminution time point and were compared with the morphological parameters of the UICC crocidolite standard, chosen here as reference sample to describe asbestos-like morphology. The morphological parameters were obtained by means of light microscopy coupled with automated image analysis (FPIA). For each time point, a representative scanning electron microscopy (SEM) image was reported for qualitative comparison. Automated analysis allows thousands of particles and fibres to be measured and a reliable statistical significance of the quantitative data was achieved.

The pie-charts (Fig. 5) highlighted that the percentage of EMPs (AR>3) remained approximately constant with the comminution time. Similarly, the percentage of EMPs negligibly varied from 68% to 65% from 3 min to 20 min of comminution, respectively. For all time points, the EMP fraction was characterised by 28–30% of respirable fibres, according to the WHO counting criteria (AR>3, L> 5 µm, D <3 µm). The percentage of EMPs for UICC crocidolite was 83%, the 47% of which consisted of respirable fibres (WHO fibres). Scatter plots visualise the size distribution of the particles and fibres detected. Probability density curves (Kernel density function) were added to the size distribution scatterplot to help the reader's eye. SEM images confirmed the presence of long, very thin elongated mineral particles having morphological and dimensional criteria similar to asbestos amphiboles. Our data support

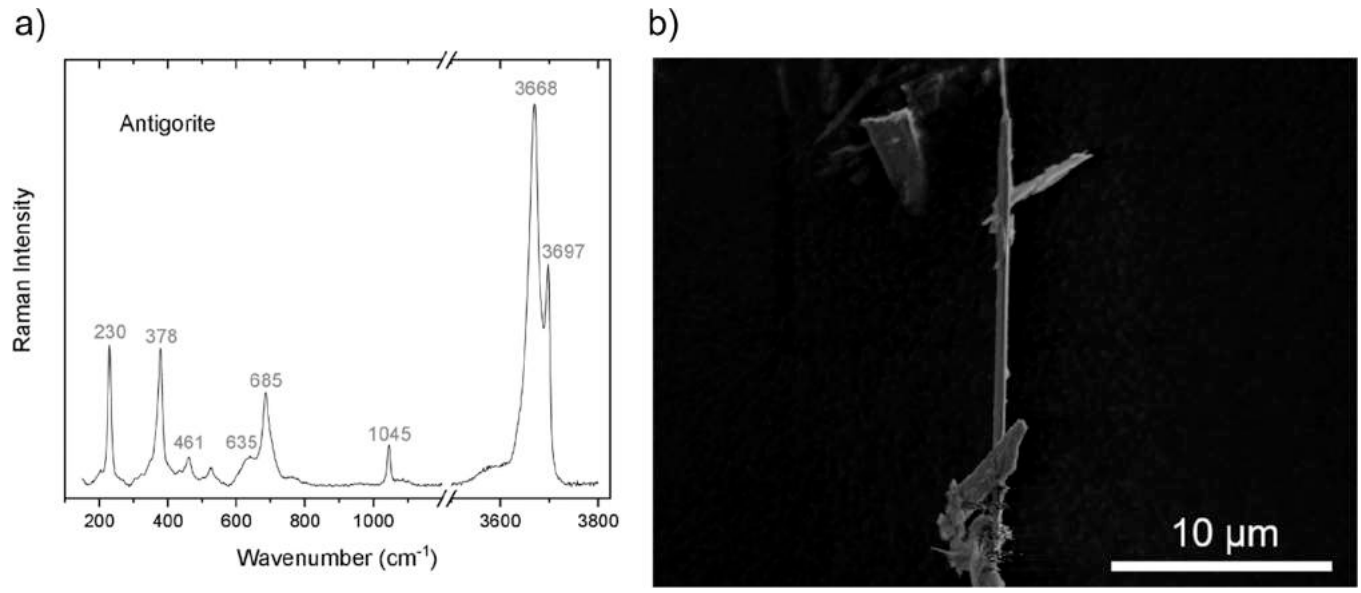

Fig. 4. Serpentine phase identification and preliminary morphological assessment. a) Representative Raman spectrum of the selected antigorite vein. Phase assignment was carried out according to Petriglieri et al. (2015) [62] and no occurrence of chrysotile or other serpentine minerals were detected. b) Representative SEM image of elongated crystal of antigorite.

the asbestos-like morphological properties of this vein of fibrous antigorite. Indeed, the high percentage of EMPs and WHO fibres, albeit lower than what was measured for standard UICC crocidolite, is largely preserved with increasing comminution times. This signals that, upon milling, our antigorite sample splits longitudinally and separates into thinner respirable fibres similarly to amphibole asbestos, rather than reducing its average length, as it would be expected for non-asbestos minerals that split perpendicularly to the c-axis and generate the so-called "cleavage fragments" [79]. A representative SEM image of milled Atg (Fig. 6) clearly highlights the fibrils that are prone to be released from a representative fibre.

3.4. Mineral structure and chemical composition

The structural mineralogical characterization of antigorite from Varenna Valley was performed by using a multi-analytical approach that includes X-Ray powder diffraction (XRPD), Transmission electron microscopy (TEM), Mössbauer spectroscopy, and Electron microprobe analysis (EMPA).

3.4.1. X-ray powder diffraction (XRPD)

XRPD data were used to define the average superstructure of antigorite by using the approach of Uehara (1998) [80]. The procedure requires the identification and measurement of the position of the first to third-order satellite reflections of the type h_s,0,1 (where $h_s = 0 \pm u/M$ and u = 1,2,3) (Fig. 7.a). In fact, the difference in the 2θ angle between 001 and ± 3/M,0,1 (the so-called Δ2θ) is modulated by the supercell M value (number of sub-cells having a parameter of ca. 5.44 Å; [81]) as it has been demonstrated that the *c* parameter and the ß angle are relatively constant in antigorite samples [80]. Data indicated that superstructure reflections were significantly broadened, confirming the coexistence of different antigorite polysomes, as revealed by TEM observations. The measured Δ2θ value of 1.42°2θ is consistent with an M value of 7.99, derived from the regression equation M = 11.42–2.41 × Δ2θ devised by Uehara (1998) [80]. In the case of M being equal to n, an integer number, the superstructure contains an odd number of tetrahedra (m) and an even number (m-1) of octahedra, where M = (m-1)/2. Therefore, the present sample is prevalently characterised by a superstructure consisting of 17 tetrahedra and 16 octahedra in the supercell, modulation that corresponds to the m = 17 antigorite polysome [82]. This polysome crystallises in the Pm space group (s.g.).

Moreover, a whole powder pattern decomposition using the Le Bail method (Le Bail et al., 1988) was performed using Topas V6 [83]. The refinement converged to the following cell parameters (s.g. *Pm*): *a* = 43.4391(4) Å, *b* = 9.25304(8) Å, *c* = 7.29217(12) Å, ß = 91.3194 (13)° in excellent agreement with those reported by Capitani and Mellini (2004) [84] for a sample from Val Malenco, Italy (Fig. 7.b).

3.4.2. Transmission electron microscopy (TEM)

The observation carried out by TEM on powdered samples revealed prismatic to fibrous antigorite crystals, in *ab* preferred orientation, elongated along their [010] axis (Supplementary Materials S4). Ion-milled samples, obtained from thin sections perpendicular to the fibre elongation, supported the current morphological data, showing the presence of possible interstitial porosity among elongated crystals (Fig. 8a). In this orientation, the antigorite observation plane broadly corresponds to *ac* (as testified by the *a*c** SAED pattern in the inset), with the long side corresponding to the [100] axis. High-resolution images revealed the common occurrence of polysynthetic twinning parallel to (001), giving rise to the characteristic chessboard nano-texture (Fig. 8b). Moreover, antigorite crystals may show polysomatic disorder, modulation dislocations and local deformation nanostructure, like layer bending, faulting, and fracturing with preferential rupture at crystal edges, parallel to (100) (Fig. 8b and c). Crystal terminations display a peculiar triangular shape (Fig. 8a,c), typically associated with amorphous to poorly crystalline material. In particular, we noticed the common occurrence of tiny smectite-like lamellae, up to 3–5 lattice fringes thick, with d spacing of ~ 14 Å (black arrows in Fig. 8c,d). Superstructure periodicity has been measured both in *a*b** and in *a*c** SAED patterns, as well as in HR images (through TEM-dedicated image analysis software). The obtained values are quite variable, remarking the possible polysomatic disorder of vein antigorite (from crystal to crystal, and within the same crystal). The overall measured range is 37.0 – 45.7 Å, even if local measures in HR images (in polysomatically-disordered portions) provided values up to 55 Å.

3.4.3. Mechanism of fibre formation of antigorite

HR-TEM observations allowed us to define the structural parameters of antigorite from Varenna Valley and to describe the mechanism of

Atg - 2 min

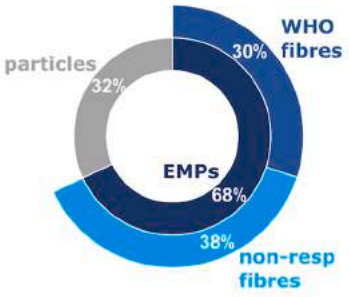

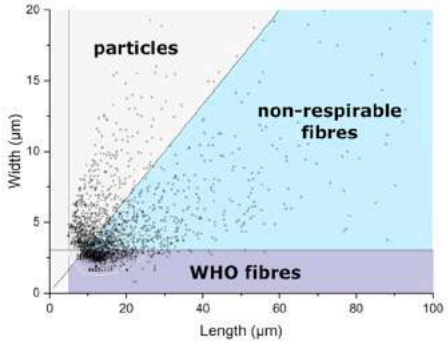

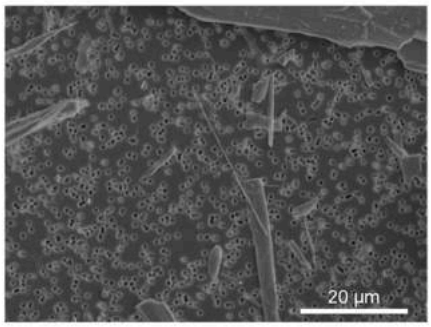

Atg - 5 min

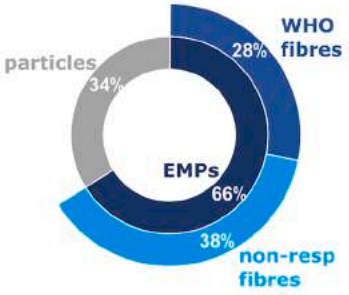

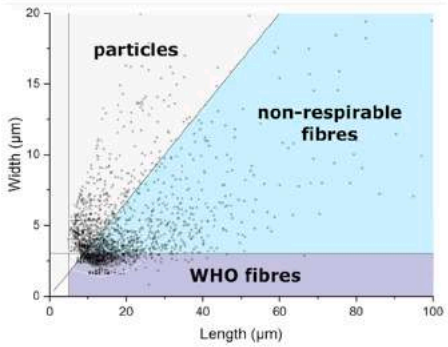

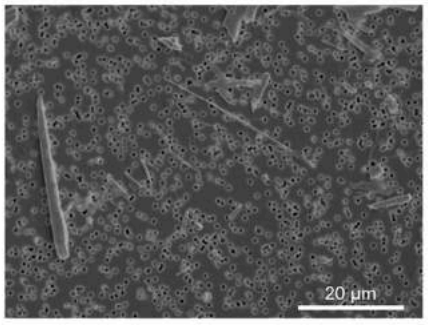

Atg - 10 min

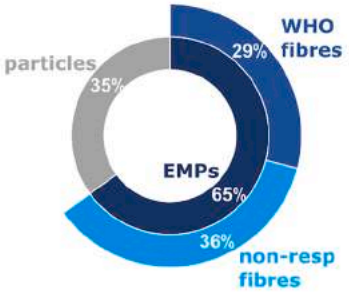

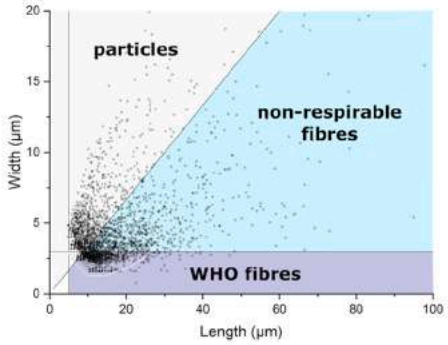

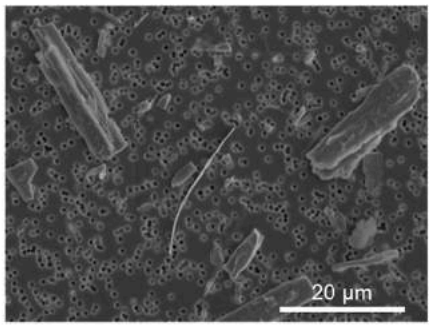

Atg - 20 min

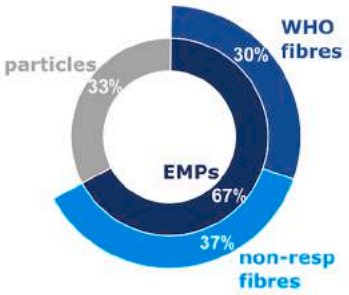

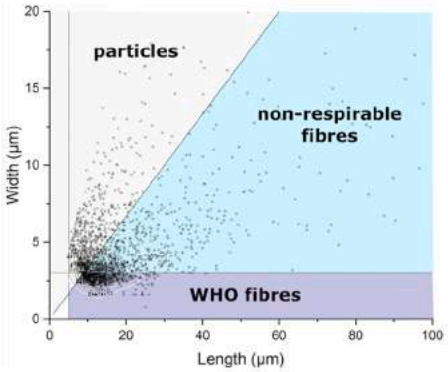

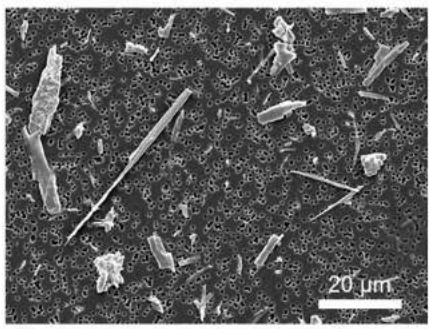

Crocidolite UICC

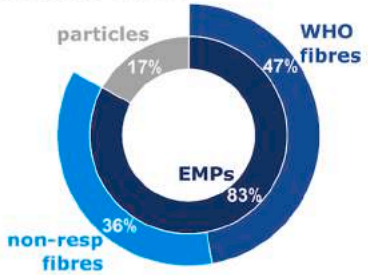

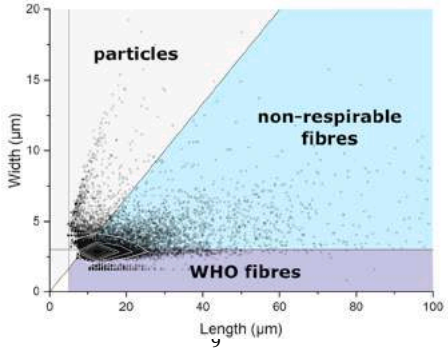

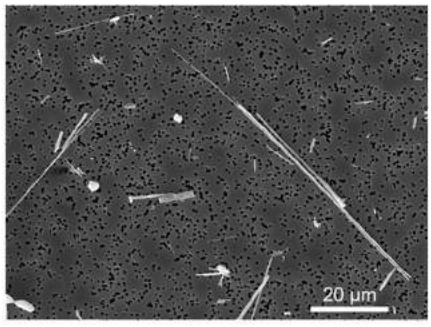

(caption on next page)

Fig. 5. Antigorite particle size distribution after standardised mechanical grinding (2, 5, 10, and 20 min) detected by optical microscopy and automated image analysis (FPIA). Doughnut pie-charts show the % of objects with AR > 3 (EMPs, according to NIOSH definition [7]) and WHO fibres (AR >3, W <3 μm, L >5 μm; [1]). Scatter plot illustrates the distribution of particles (AR <3; grey field), non-respirable fibres (AR >3; W >3 μm; light-blue field), and WHO fibres (AR >3, W <3 μm, L > 5 μm; blue field). Density curves (black to white lines) visualise the distribution of particle populations in the dataset. Representative SEM images of comminuted antigorite show the asbestos-like morphology. Crocidolite UICC was added for comparison. FPIA images are reported in Supplementary Materials S3.

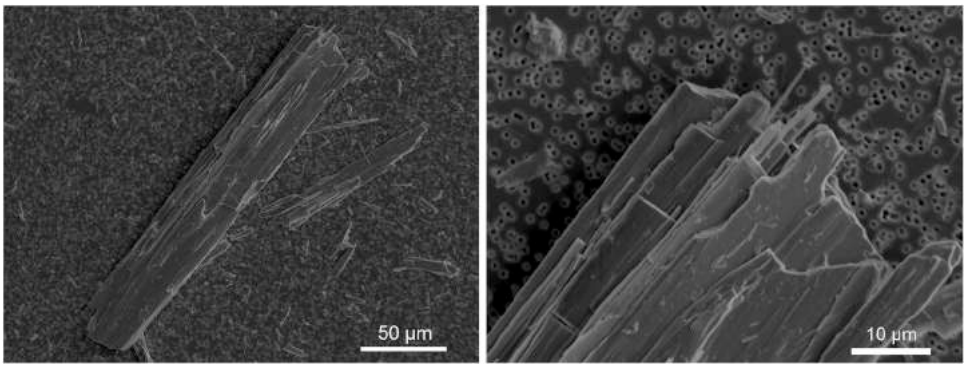

Fig. 6. – Representative SEM images of an Atg bundle showing the typical asbestos-like breakage of crystals along the growth direction axes.

formation of EMPs and fibres. Those nanostructural considerations were used to support the asbestos-like morphology of the antigorite described in this work. The splintery-fibrous texture of antigorite veins is due to the preferred orientation of antigorite crystals, elongated along [010]. Shear direction corresponds to antigorite [010] (i.e., the longest side of antigorite crystals) as displayed in 3D drawing in Fig. 9 [22,85]. Overall observations, from the outcrop down to the micro-nano scale, revealed possible misalignment of [010] axes, due to the possible slight changes in the overall shear direction within the vein. One of the most important implications of antigorite preferred orientation is that (001) cleavage planes are always parallel to shear direction, thus resulting in a deformation-induced grain size reduction with progressive delamination parallel to (001) [22]. Observations on cross-vein sections revealed that antigorite crystals (observed in their *ac* planes; Fig. 9) display rotational disorder around [010]. The long side of antigorite *ac* sections is parallel to (001) and corresponds to the orientation of polysynthetic twinning planes. TEM observations revealed preferential rupture parallel to (100), that typically occur at crystal edges and at crystal structural defects (such as dislocation of modulation or unusually large polysomes). The preferential rupture parallel to (100), coupled with easy (001) delamination, is responsible for a progressive shear-enhanced evolution of the antigorite crystal habit, from prismatic to fibrous. This pervasive process of grain size reduction, with rupture parallel to both (100) and (001), determines the generation of delaminated crystals with sub-micrometer diameter and the formation of asbestos-like elongated structures.

3.4.4. Mössbauer spectroscopy

The ^{57}Fe Mössbauer spectrum of the antigorite from Varenna Valley (Fig. 10) showed one doublet with a large quadrupole splitting (QS), typical for Fe^{2+}, and one superimposed doublet with a smaller quadrupole splitting, typical for Fe^{3+}. The spectrum was first fitted with one set each for the two doublets, following previous fitting models [86,87], resulting in hyperfine parameters in close agreement with the values earlier reported. However, this two-doublet fit showed some misfit of the Fe^{2+} doublet, and hence another doublet in the Fe^{2+} range was added which resulted in a significantly better fit. The two Fe^{2+} doublets showed a small difference in isomer shift (IS) and a larger difference in quadrupole splitting (Fig. 10), which may be attributed to next-nearest neighbour effects involving Mg, Fe^{2+} and Fe^{3+}. Assuming similar recoil-free fraction for Fe^{2+} and Fe^{3+}, the Fe^{3+}/Fe_{tot} ratio obtained from area measurement was 0.31. The broad envelope of the Fe^{3+} doublet indicates the possible presence of both tetrahedrally and octahedrally coordinated Fe^{3+}, but it was not possible to resolve the doublets by curve fitting, due to limited spectral resolution.

3.4.5. Electron microprobe analysis (EMPA)

The average chemical composition is shown in Table 1. EMPA analyses suggest chemical homogeneity of the elongated crystals, being differences for major elements below 5% relative. Comparison with chemical data obtained by Groppo and Compagnoni (2007) [73] on fibrous antigorite from Lanzo Ultramafic Massif (Western Alps, Italy) highlighted significant differences only in the Al content, (ca. 0.12 apfu for Lanzo Massif antigorites vs ca. 0.07 apfu for and Varenna Valley antigorite). Fe^{2+}/Fe^{3+} partition was performed using the Fe^{3+}/Fe_{tot} ratio of 0.31 obtained by Mössbauer spectroscopy. In the absence of clear indication, all Fe^{3+} was allocated at the octahedral layer. The formula was normalised based on 8.647 oxygen atoms. This value derives from the general empirical formula of antigorite reported by Kunze (1961) [88]:

$$^{VI}M^{IV}_{3\ m-3}T_{2\ m}O_{5\ m}(OH)_{4\ m-6}$$

with M = Mg, Fe, Ni, Al; T = Si, Al; m = number of unique tetrahedra along the modulation wavelength and was calculated assuming a representative m = 17 based on XRPD data. As can be seen, there is excellent agreement with the ideal formula. Owing to the occurrence of < 2 apfu, Si and Al were partitioned between the tetrahedral and octahedral layers.

3.5. Durability of antigorite in mimicked Gamble's solution (MGS)

The durability of antigorite fibres incubated in a mimicked Gamble's solution at pH 4.5 for 1, 24, and 168 h was evaluated by inductively coupled plasma - optical emission spectroscopy (ICP-OES), specifically reporting i) the cation release as a function of incubation time, and ii) the congruent or incongruent dissolution of the mineral. Data acquired on antigorite were compared with UICC chrysotile, leached under the same experimental conditions. The chemical alterations and the iron speciation induced by incubation in MGS were described by means of X-ray photoemission spectroscopy (XPS), qualitatively and quantitatively.

3.5.1. Inductively coupled plasma - optical emission spectroscopy (ICP - OES)

The kinetics of silicon and magnesium release from antigorite as a function of time over a period of 1 week (168 h) is reported in Fig. 11a. Details on minor occurrence of Fe and Al are available in the

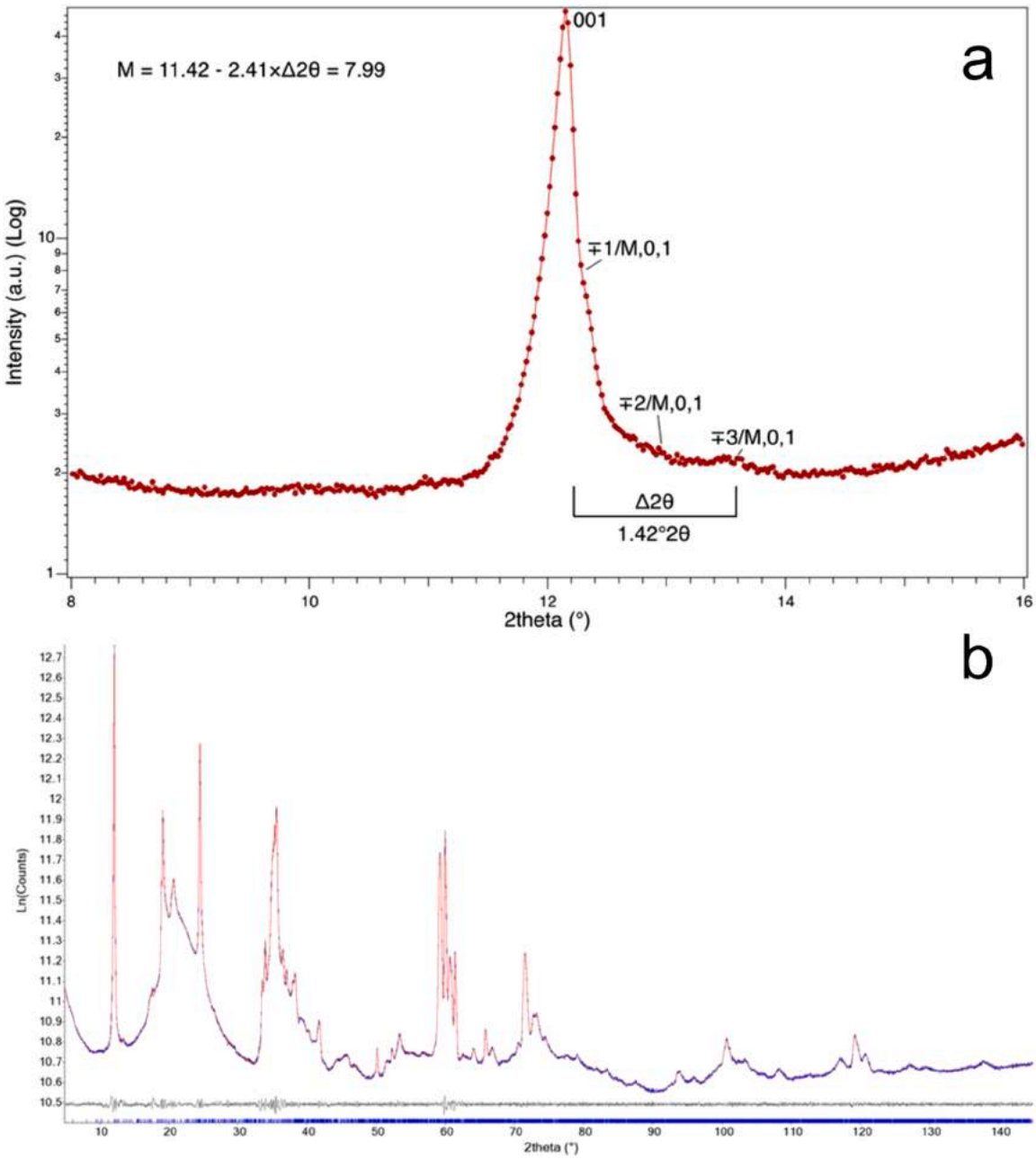

Fig. 7. a) Magnified view of the diffraction pattern (intensity shown in logarithmic scale). Position of the first to third-order superstructure reflections is indicated; b) Plots of the Le Bail refinement (intensity in logarithmic natural scale). Blue: experimental; red: calculated; grey: difference; vertical bars: position of the calculated Bragg reflections of the antigorite m = 17 polysome (s.g. *Pm*).

Supplementary materials, Fig. S5. Results showed that the release of these cations progressively increased with incubation time. Specifically, Mg peaked from 639(18) mg/kg after 1 h to 1692(20) mg/kg after 1 week of dissolution time, and Si from 293(21) mg/kg to 1320(26) mg/kg in the same range of time (Fig. 11a). Al and Fe were also released in a time-depended manner up to 24 h and a plateau was reached (Fig. S5). Interestingly, UICC chrysotile released a much higher amount of both Mg and Si, that ranged from 5182 mg/kg and 1712 mg/kg (after 1 h of incubation) up to 12,842 mg/kg and 5588 mg/kg (after 24 h), respectively. For longer incubation times, the amount of leached Mg and Si slightly decreases, suggesting that a steady state was reached (Fig. 11a). Negligible amounts of Al and Fe were leached out also of chrysotile after 24 h of incubation (Fig. S5). Both samples released ions mainly in the first 24 h of incubation, suggesting that fibre solubility is more favourable under higher undersaturation conditions. Accordingly, after 24 h a near-saturation condition hinders the element release from the fibre surface to the media. This event is particularly evident for chrysotile for which we even observed a decrease in Mg and Si release for longer incubation times, likely related to the formation of neo-formed precipitates. It is worth noting that XRPD analysis did not highlight any occurrence of new phases in the incubated samples, suggesting that the neo-formed precipitate/s are possibly amorphous. The metal release observed in the first 24 h is likely enhanced by the presence of citrate ($Na_3C_6H_5O_7$) in the leaching solution, which acts as a chelating agent having four groups (three carboxyl and one hydroxyl group) able to bind metal ions [89].

In order to compare the solubility of antigorite with UICC chrysotile, the release of Si was normalised to surface area (SSA Kr-BET = 5.7 m^2/

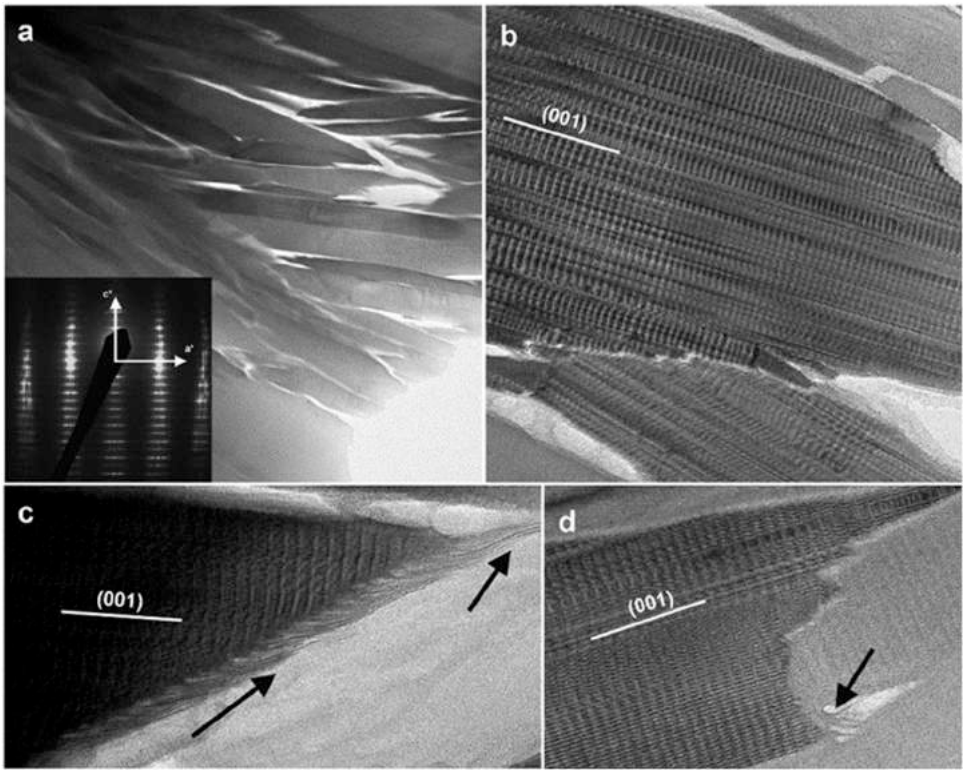

Fig. 8. HR-TEM representative images of the selected antigorite vein. a) Bright field image of an ion-milled sample obtained from cross sections of the vein. Inset: *a*c** SAED pattern; b) high-resolution image revealing polysynthetic twinning parallel to (001); c) and d) crystal terminations showing smectite-like lattice fringes indicated by black arrows.

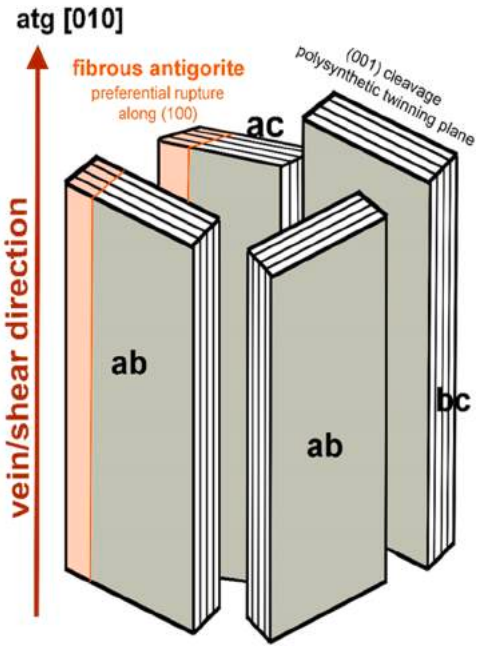

Fig. 9. 3D drawing describing the mechanism formation of sub-micrometer fibre diameter asbestos-like antigorite. In this orientation, the *ab* planes of antigorite are parallel to the shear direction [010], displaying a rotational disorder around [010]. The preferential rupture responsible for fibre formation occurs along (100).

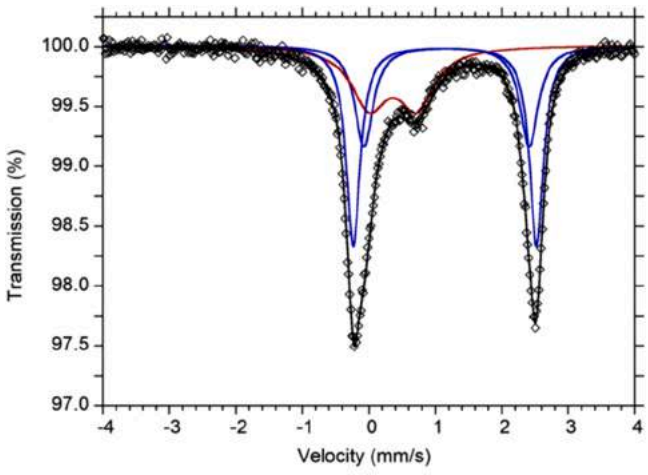

IS (mm/s)	QS (mm/s)	FWHM	Area (%)	Assignment
1.139(2)	2.76(1)	0.25(2)	42(4)	Fe^{2+}
1.164(6)	2.49(4)	0.33(3)	28(5)	Fe^{2+}
0.36(2)	0.71(3)	0.65(4)	31(3)	Fe^{3+}

Fig. 10. ^{57}Fe Mössbauer spectrum and parameters of antigorite obtained at room-temperature. Fitted absorption doublets assigned to Fe^{2+} are indicated in blue and Fe^{3+} in red. Diamonds denote the measured spectrum, and black curve represents the summed fitted spectrum. Isomer shift (IS) quadrupole splitting (QS), peak FWHM and Area% for the three assigned Fe species is reported in the bottom table.

g). Si release was considered as it represents the rate determining step for silicate dissolution [90]. The maximum value of normalized Si released was 233(5) mg/m^2 and 378(2) mg/m^2, for antigorite and chrysotile respectively (Fig. S5) revealed that chrysotile dissolves to a greater extent than antigorite, under the experimental conditions

Table 1
Chemical composition obtained by EMPA on 10 analytical points, expressed by oxides, observed min-max ranges and empirical formulas as atoms per formula unit (apfu).

				Antigorite	ideal
Oxides	wt%	Range	Sites	apfu	apfu
SiO_2	42.47(45)	41.79–43.02	Si	1.973	
Al_2O_3	1.36(7)	1.26–1.51	^{IV}Al	0.027	
MgO	37.87(48)	37.15–38.75	∑T	2	2
MnO	0.15(3)	0.11–0.21			
FeO_{tot}	3.08(7)	2.95–3.19	^{IV}Al	0.047	
$*H_2O$	11.76		Mg	2.622	
Total	96.67		Mn	0.006	
			Fe^{2+}	0.083	
			Fe^{3+}	0.037	
**FeO	2.12		∑M	2.795	2.823
**Fe_2O_3	1.06				
			O	5	5
			OH	3.647	3.647

Note: estimated standard deviation in brackets. Ideal refers to the empirical ideal formula of the sub-cell of a m = 17 antigorite polysome based on $^{VI}M_{3\ m\text{-}3}{}^{IV}T_{2\ m}O_{5\ m}(OH)_{4\ m\text{-}6}$ [88].* Calculated from stoichiometry.** Measured by Mössbauer spectroscopy (see Fig. 10).

adopted. The higher solubility showed by chrysotile could be even higher in biological environment, where chelating molecules are continuously renewed, and saturation and reprecipitation are less likely to occur.

Fig. 11b shows the variation of Si/Mg ratio for antigorite and chrysotile as a function of the incubation time. To help reader eye, the theoretical Si/Mg ratio, calculated from the bulk chemical analyses reported in the previous paragraph, is reported (dotted line). Antigorite is characterised by a transient incongruent dissolution ratio, with Mg exceeding Si during the initial dissolution steps. After a few hours of incubation, the Si/Mg leaching ratio stabilizes to a rather congruent cation release (experimental Si/Mg = 0.68 with respect to a theoretical value of 0.75). On the contrary, Si and Mg leaching is strongly incongruent in chrysotile, independently with leaching time. In particular, chrysotile showed a preferential release of the octahedrally coordinated Mg with respect to the tetrahedral Si, in agreement with their differences in Madelung site energy [91] and experimental dissolution rates [92]. On these bases, the lower dissolution rate of antigorite with respect to chrysotile might be due to more effective interlayer interactions occurring in antigorite [82]. After the first steps of incongruent dissolution, the leaching of antigorite proceeded in a congruent and limited manner, as the result of the higher stability of the SiO_4 layer. This suggests a higher biodurability of antigorite than chrysotile, consistently with previous observation on antigorite specimen leached in phagolysosomal simulating fluid (PSF, pH 4.5) and the Gamble's solution (pH 7.4) [12].

3.5.2. *X-ray photoelectron spectroscopy (XPS)*

Pristine and incubated antigorite and UICC chrysotile were investigated for chemical changes that could have occurred at the fibres surface. The results are reported in Table 2. Survey spectra of pristine and one-week incubated samples are shown in Fig. S6. No significant differences were observed between the incubated and the pristine samples of antigorite, in agreement with its congruent dissolution. Conversely, one week-incubated chrysotile showed a clear Fe enrichment with respect to the other cations, in accordance with ICP-OES results that indicate low Fe release in the adopted experimental conditions.

For antigorite, the amount of Fe content allowed the fitting of the high-resolution Fe 2p3/2 signal by applying the approach used in Fantauzzi et al. [50,51] and Pacella et al. [32,33]. Pristine sample showed a more oxidised surface (60% Fe(III) with respect to the bulk 30% Fe(III) evidenced by Mössbauer data), with Fe(III) present as oxide (Fe_2O_3) and oxyhydroxide (FeOOH) species, likely due to weathering processes [50,51]. In addition, the sample incubated for one week in the Gamble's solution shows a significant increase of the FeOOH component at the expense of the Fe(III)-O component, with respect to the pristine one (Table 2). This is likely due to the low solubility of antigorite sample, which hinders the occurrence on the fibre surface of new iron centres from the bulk (in the form of Fe(II)-O and Fe(III)-O), promoting therefore the growth of the FeOOH layer on the surface of the fibre. Similar results were obtained on tremolite samples immersed in acidic MGS: in that case, iron oxidation was faster than the leaching of the fibrous mineral due to the low solubility of tremolite, thus an increase of the FeOOH % upon leaching time was observed [34].

3.6. *Surface reactivity in free radical release*

Surface reactivity was evaluated by checking the ability of antigorite to catalyse the release of radical species. Two mechanisms of free radical generation were investigated: i) carboxyl radical ($^{\bullet}COO^{-}$) release from

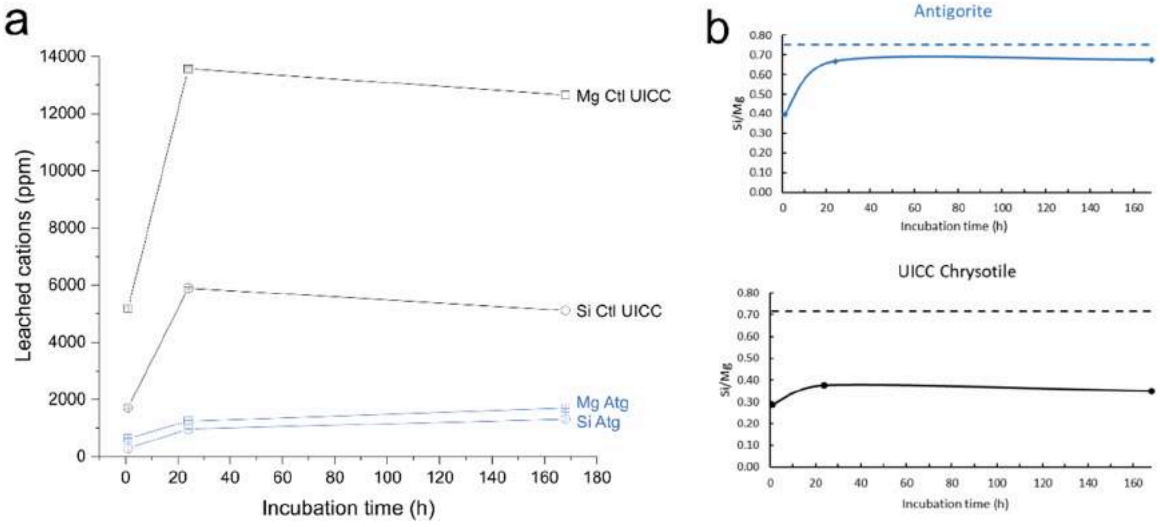

Fig. 11. Durability of antigorite from Varenna Valley. a) Si and Mg release from Atg (blue) and UICC chrysotile (black) during incubation in MGS as a function of time (squares = Mg, circles = Si) by after incubation. The dissolution was evaluated at 37 °C, by static tests. The quantity of ions released in solution was measured by ICP-OES after 1, 24, and 168 h of incubation. Experiments were performed in quadruplicate. Values are reported as means ± SD. b) variation of the Si/Mg ratio of the released cations at each time of sampling as compared to that of the bulk (dotted line) arising from chemical analyses of the pristine sample.

Table 2
Composition (at%) of antigorite and UICC chrysotile by XPS before (pristine sample) and after dissolution in MGS at acidic pH for 1 week (1 W). For antigorite the relative intensities of the components of Fe 2p3/2 identified by curve-fitting are also reported. Due to the low signal-to-noise ratio the curve fitting of Fe 2p3/2 of chrysotile samples was not performed. Mean values on three independent measurements are listed together with standard deviations (in parentheses).

	Composition (at%)				Fe speciation (%)		
Samples	O	Si	Mg	Fe	Fe (II)-O	Fe (III)-O	Fe (III)-OOH
Atg - Pristine	60(2)	19 (1)	20 (1)	1.0 (0.2)	41(2)	20(1)	39(3)
Atg - 1 W	58(1)	19 (1)	22 (2)	1.0 (0.3)	40(5)	10(2)	50(3)
UICC Ctl - Pristine	61.8 (0.1)	14 (1)	24 (1)	0.2 (0.1)	n.d.	n.d.	n.d.
UICC Ctl - 1 W	63.0 (0.2)	13 (1)	23 (1)	1.0 (0.2)	n.d.	n.d.	n.d.

the formate ion ($HCOO^-$), used as a model target molecule for homolytic cleavage of a carbon-hydrogen bond in organic molecules and ii) hydroxyl radical ($^{\bullet}OH$) release in the presence of H_2O_2, used as a probe for Fe-induced Fenton-like activity. UICC chrysotile was used as reference sample.

Antigorite was reactive in both carboxyl (Fig. 12 A) and hydroxyl radical (Fig. 12B) generation. The production of carboxyl radicals was observed only in a reducing environment (presence of ascorbic acid), also for chrysotile.

The hydroxyl radical yield was quantified after incubation in the MGS at acid pH performing a double integration of the EPR signals (Fig. 12 C). The potency of antigorite to catalyse $^{\bullet}OH$ slightly increased with leaching time, from 0 (pristine) to 168 h. This may be due to the fibre leaching promoting coordinative unsaturation of the surface Fe centres as proposed in previous work on amphibole surface reactivity [93]. An opposite trend was observed for chrysotile, which showed a quite different surface reactivity from antigorite. The time-dependent decrease of the $^{\bullet}OH$ radicals generated by pristine and leached chrysotile confirmed that radical yield is not directly correlated to the overall amount of Fe content. In fact, XPS data indicate an enrichment in iron species with leaching time. However, the newly formed species, especially highly aggregated species such as iron oxides and oxy-hydroxide are generally held less reactive in Fenton-like processes than well dispersed ions [41,94,95]. In the case of leached chrysotile, the reduction of Fenton-like reactivity might be due to the progressive growth of precipitates on the fibre surface that prevent the interaction between Fe reactive sites and hydrogen peroxide molecules.

4. Conclusions

This work reports about an interdisciplinary approach for the characterization of an asbestos-like antigorite from a natural site, aiming to evaluate its potential health and environmental hazard. A NOA site with the occurrence of a macroscopically elongated, potentially hazardous antigorite was described. Potentially asbestos-like antigorite was sampled considering the structural and geological information made available by field and petrographic analyses. A representative vein was selected, and the sample was investigated for the key morphometric, structural, and chemical parameters that are relevant in particle toxicity. Specifically, the antigorite morphology, crystal-chemistry, crystal-structure, dissolution pathway, and surface reactivity were evaluated and compared with UICC chrysotile asbestos. Overall, the data acquired signalled the potential hazard of antigorite. Upon mechanical stress, the sample was able to release up to 67% of EMPs, of which 30% of respirable fibres, according to the WHO counting criteria. TEM investigation highlighted that the grain size reduction determining sub-micrometer fibres is due to a preferential rupture parallel to (100) coupled with easy (001) delamination. Antigorite fibres showed a durability higher that UICC chrysotile in MGS and the free-radical yield increased with leaching time.

Future investigations on the in vitro cytotoxicity and genotoxicity of the selected antigorite fibres are being carried out, to complete the toxicological assessment of the antigorite from Varenna Valley, Italy. The approach described here might be easily adapted to the plethora of fibrous minerals, NOA and EMPs, which hazardous effects are currently debated.

Environmental implications

Health and environmental protection agencies are concerned by the potential hazard posed by natural occurrence of asbestos and elongated mineral particles. New tools for the risk assessment of the natural occurrence of asbestos-like minerals are highly demanded. We describe here a multidisciplinary approach that encompasses hazard investigation from field to nanostructural analyses and paves the way to a widely applicable method for the identification of a potentially hazardous asbestos-like mineral in a natural site. An antigorite vein was selected and investigated. Its key toxicologically relevant properties signal a possible concern for human health and the environment.

Declaration of Competing Interest

The authors declare that they have no known competing financial interests or personal relationships that could have appeared to influence the work reported in this paper.

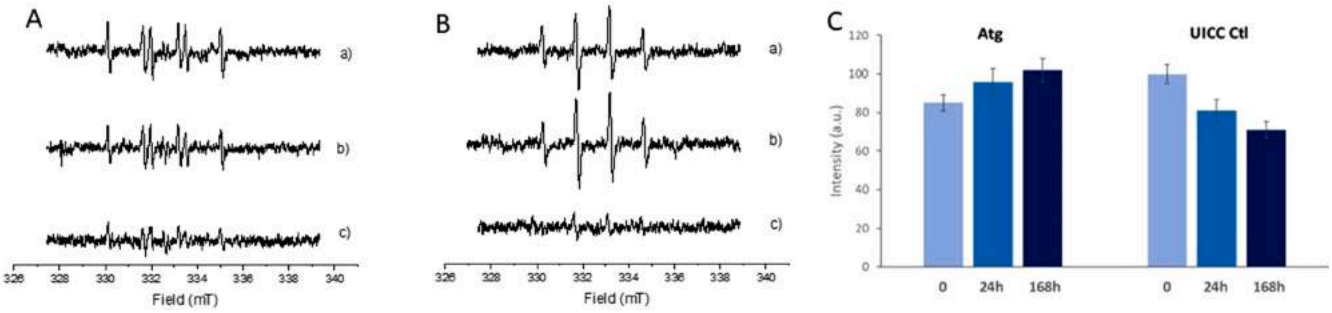

Fig. 12. Representative EPR spectra of (A) $[DMPO\text{-}COO^-]^{\bullet}$ and (B) $[DMPO\text{-}OH]^{\bullet}$ adducts obtained from (a) antigorite, (b) UICC chrysotile A, and c) blank recorded after 60 and 30 min of incubation with $HCOO^-$ and H_2O_2 as target molecules, respectively. The $[DMPO\text{-}COO^-]^{\bullet}$ and the $[DMPO\text{-}OH]^{\bullet}$ adduct signal is characterized by a six and four line spectrum with intensity 1: 2: 2: 1, respectively. In the panel A, the weak doublet at the centre of the field (ca. 333 mT) is due to the formation of the ascorbyl radical from the reaction of ascorbic acid, used here as reductant for iron at mineral surface. The quantification of the $[DMPO\text{-}OH]^{\bullet}$ signal generated after 1 and 7 days of incubation in MGS at acid pH is reported in panel C).

Data availability

Data will be made available on request.

Acknowledgements

This work was funded by the INAIL - BRIC 2019 project (grant number ID 57.1). FT and MT acknowledge support from the Project CH4.0 under the MUR program "Dipartimenti di Eccellenza 2023–2027" (CUP: D13C22003520001). Micro-Raman spectra have been obtained with the equipment acquired by the Interdepartmental Centre "G. Scansetti" for Studies on Asbestos and Other Toxic Particulates with a grant from Compagnia di San Paolo, Torino, Italy. Pierluigi Canepa (OMT, Quart, AO) and Domenico Mannetta (Sapienza University of Rome) are thanked for the skilful realisation of the petrographic thin sections. Marcello Serracino is kindly acknowledged for technical assistance for electron microprobe analysis (EMPA) at "Istituto di Geologia Ambientale e Geoingegneria" of the National Resarch Council" (IGAG-CNR), Rome, Italy.

Appendix A. Supporting information

Supplementary data associated with this article can be found in the online version at doi:10.1016/j.jhazmat.2023.131754.

References

[1] WHO, Determination of airborne fibre number concentrations. A recommended method, by phase-contrast optical microscopy (membrane filter method)., Geneva, 1997. https://doi.org/ISBN9241544961.
[2] USGS, Asbestos statistics and information, Washington, USA, 2022. ⟨https://pubs.usgs.gov/periodicals/mcs2022/mcs2022-asbestos.pdf⟩ (accessed March 22, 2023).
[3] Stayner, L., Welch, L.S., Lemen, R., 2013. The worldwide pandemic of asbestos-related diseases. Annu Rev Public Health 34, 205–216. https://doi.org/10.1146/annurev-publhealth-031811-124704.
[4] IARC, Monographs on the Evaluation of Carcinogenic Risks to Humans. Arsenic, Metals, Fibres, and Dusts. A review of human carcinogens., Lyon, France, 2012.
[5] Thives, L.P., Ghisi, E., Thives Júnior, J.J., Vieira, A.S., 2022. Is asbestos still a problem in the world? A current review. J Environ Manag 319. https://doi.org/10.1016/j.jenvman.2022.115716.
[6] Cullinan, P., Muñoz, X., Suojalehto, H., Agius, R., Jindal, S., Sigsgaard, T., Blomberg, A., Charpin, D., Annesi-Maesano, I., Gulati, M., Kim, Y., Frank, A.L., Akgün, M., Fishwick, D., de la Hoz, R.E., Moitra, S., 2017. Occupational lung diseases: from old and novel exposures to effective preventive strategies. Lancet Respir Med 5, 445–455. https://doi.org/10.1016/S2213-2600(16)30424-6.
[7] NIOSH, Asbestos Fibers and Other Elongate Mineral Particles: State of the Science and Roadmap for Research., 2011. ⟨http://www.cdc.gov/niosh/docs/2011–159/pdfs/2011–159.pdf%5Cnhttp://www.cdc.gov/niosh/docs/2011–159/⟩.
[8] Boffetta, P., Mundt, K.A., Thompson, W.J., 2018. The epidemiologic evidence for elongate mineral particle (EMP)-related human cancer risk. Toxicol Appl Pharm 361, 100–106. https://doi.org/10.1016/j.taap.2018.09.021.
[9] Garabrant, D.H., Pastula, S.T., 2018. A comparison of asbestos fiber potency and elongate mineral particle (EMP) potency for mesothelioma in humans. Toxicol Appl Pharm 361, 127–136. https://doi.org/10.1016/j.taap.2018.07.003.
[10] Harper, M., 2008. 10th anniversary critical review: naturally occurring asbestos. J Environ Monit 10, 1394–1408. https://doi.org/10.1039/b810541n.
[11] Cardile, V., Lombardo, L., Belluso, E., Panico, A., Capella, S., Balazy, M., 2007. Toxicity and carcinogenicity mechanisms of fibrous antigorite. Int J Environ Res Public Health 4, 1–9. https://doi.org/10.3390/ijerph2007010001.
[12] Gazzano, E., Petriglieri, J.R., Aldieri, E., Fubini, B., Laporte-Magoni, C., Pavan, C., Tomatis, M., Turci, F., 2022. Cytotoxicity of fibrous antigorite from New Caledonia. Environ Res, 115046. https://doi.org/10.1016/j.envres.2022.115046.
[13] ANSES, Évaluation de la toxicité de l'antigorite., Maisons-Alfort, France, 2014.
[14] Lee, R.J., Strohmeier, B.R., Bunker, K.L., Van Orden, D.R., 2008. Naturally occurring asbestos - A recurring public policy challenge. J Hazard Mater 153, 1–21. https://doi.org/10.1016/j.jhazmat.2007.11.079.
[15] Koumantakis, E., Kalliopi, A., Dimitrios, K., Gidarakos, E., 2009. Asbestos pollution in an inactive mine: determination of asbestos fibers in the deposit tailings and water. J Hazard Mater 167, 1080–1088.
[16] Freemantle, G.G., Chetty, D., Olifant, M., Masikhwa, S., 2022. Assessment of asbestos contamination in soils at rehabilitated and abandoned mine sites, Limpopo Province, South Africa. J Hazard Mater 429. https://doi.org/10.1016/j.jhazmat.2021.127588.
[17] Malinconico, S., Paglietti, F., Serranti, S., Bonifazi, G., Lonigro, I., 2022. Asbestos in soil and water: a review of analytical techniques and methods. J Hazard Mater 436. https://doi.org/10.1016/j.jhazmat.2022.129083.
[18] Walter, M., Geroldinger, G., Gille, L., Kraemer, S.M., Schenkeveld, W.D.C., 2022. Soil-pH and cement influence the weathering kinetics of chrysotile asbestos in soils and its hydroxyl radical yield. J Hazard Mater 431. https://doi.org/10.1016/j.jhazmat.2021.128068.
[19] Bailey, K., Chatfield, E., Gibbs, G., Wylie, A., 2018. Universe of Particles. Toxicol Appl Pharm 361, 185. https://doi.org/10.1016/j.taap.2018.07.027.
[20] Vignaroli, G., Rossetti, F., Belardi, G., Billi, A., 2011. Linking rock fabric to fibrous mineralisation: a basic tool for the asbestos hazard. Nat Hazards Earth Syst Sci 11, 1267–1280. https://doi.org/10.5194/nhess-11-1267-2011.
[21] Botta, S., Avataneo, C., Barale, L., Compagnoni, R., Cossio, R., Marcelli, I., Piana, F., Tallone, S., Turci, F., 2020. Petrofacies for the prediction of NOA content in rocks: application to the "Gronda di Genova" tunneling project. Bull Eng Geol Environ 79, 185–204. https://doi.org/10.1007/s10064-019-01539-6.
[22] Viti, C., Collettini, C., Tesei, T., Tarling, M.S., Smith, S.A.F., 2018. Deformation processes, textural evolution and weakening in retrograde serpentinites. Minerals 8. https://doi.org/10.3390/min8060241.
[23] Donaldson, K., Seaton, A., 2012. A short history of the toxicology of inhaled particles. Part Fibre Toxicol 9. https://doi.org/10.1186/1743-8977-9-13.
[24] Turci, F., Tomatis, M., Pacella, A., 2017. Surface and bulk properties of mineral fibres relevant to toxicity. Eur Mineral Union Notes Mineral, Mineral Soc 171–214. https://doi.org/10.1180/EMU-notes.18.6.
[25] Gualtieri, A.F., 2023. Journey to the centre of the lung. The perspective of a mineralogist on the carcinogenic effects of mineral fibres in the lungs. J Hazard Mater 442. https://doi.org/10.1016/j.jhazmat.2022.130077.
[26] Ballirano, P., Bloise, A., Gualtieri, A.F., Lezzerini, M., Pacella, A., Perchiazzi, N., Dogan, M., Dogan, A.U., 2017. The crystal structure of mineral fibres. In: Gualtieri, A.F. (Ed.), Mineral Fibres: Crystal Chemistry, Chemical Physical Properties, Biological Interaction and Toxicity, EMU Notes. European Mineralogical Union and the Mineralogical Society of Great Britain & Ireland, UK, pp. 17–64. https://doi.org/10.1180/EMU-notes.18.2.
[27] Korchevskiy, A.A., Wylie, A.G., 2022. Dimensional characteristics of the major types of amphibole mineral particles and the implications for carcinogenic risk assessment. Inhal Toxicol 34, 24–38. https://doi.org/10.1080/08958378.2021.2024304.
[28] Wylie, A.G., Bailey, K.F., Kelse, J.W., Lee, R.J., 1993. The importance of width in asbestos fiber carcinogenicity and its implications for public policy. Am Ind Hyg Assoc J 54, 239–252. https://doi.org/10.1080/15298669391354621.
[29] Wylie, A.G., Korchevskiy, A.A., Van Orden, D.R., Chatfield, E.J., 2022. Discriminant analysis of asbestiform and non-asbestiform amphibole particles and its implications for toxicological studies. Comput Toxicol 23. https://doi.org/10.1016/j.comtox.2022.100233.
[30] Stanton, M.F., Layard, M., Tegeris, A., Miller, E., May, M., Morgan, E., Smith, A., 1981. Relation of Particle Dimension to Carcinogenicity in Amphibole Asbestoses and Other Fibrous Minerals. JNCI: J Natl Cancer Inst 67, 965–975. https://doi.org/10.1093/jnci/67.5.965.
[31] Meeker, G.P., Bern, A.M., Brownfield, I.K., Lowers, H.A., Sutley, S.J., Hoefen, T.M., Vance, J.S., 2003. The composition and morphology of amphiboles from the Rainy Creek complex, near Libby, Montana. Am Mineral 88, 1955–1969. https://doi.org/10.2138/am-2003-11-1239.
[32] Pacella, A., Fantauzzi, M., Turci, F., Cremisini, C., Montereali, M.R., Nardi, E., Atzei, D., Rossi, A., Andreozzi, G.B., 2014. Dissolution reaction and surface iron speciation of UICC crocidolite in buffered solution at pH 7.4: A combined ICP-OES, XPS and TEM investigation. Geochim Cosmochim Acta 127, 221–232. https://doi.org/10.1016/j.gca.2013.11.035.
[33] Pacella, A., Fantauzzi, M., Turci, F., Cremisini, C., Montereali, M.R., Nardi, E., Atzei, D., Rossi, A., Andreozzi, G.B., 2015. Surface alteration mechanism and topochemistry of iron in tremolite asbestos: A step toward understanding the potential hazard of amphibole asbestos. Chem Geol 405, 28–38. https://doi.org/10.1016/j.chemgeo.2015.03.028.
[34] Pacella, A., Ballirano, P., Fantauzzi, M., Rossi, A., Nardi, E., Capitani, G., Arrizza, L., Montereali, M.R., 2021. Surface and bulk modifications of amphibole asbestos in mimicked gamble's solution at acidic PH. Sci Rep 11. https://doi.org/10.1038/s41598-021-93758-9.
[35] Pacella, A., Ballirano, P., Fantauzzi, M., Rossi, A., Viti, C., Arrizza, L., Nardi, E., Caprioli, R., Montereali, M.R., 2021. Surface and bulk modifications of fibrous erionite in mimicked gamble's solution at acidic ph. Minerals 11. https://doi.org/10.3390/min11090914.
[36] Echigo, T., Aruguete, D.M., Murayama, M., Hochella, M.F., 2012. Influence of size, morphology, surface structure, and aggregation state on reductive dissolution of hematite nanoparticles with ascorbic acid. Geochim Cosmochim Acta 90, 149–162. https://doi.org/10.1016/j.gca.2012.05.008.
[37] Bernstein, D., Castranova, V., Donaldson, K., Fubini, B., Hadley, J., Hesterberg, T., Kane, A.B., Lai, D., McConnell, E.E., Muhle, H., Oberdörster, G., Olin, S., Warheit, D.B., 2005. Testing of fibrous particles: Short-term assays and strategies - Report of an ILSI Risk Science Institute Working Group. Inhal Toxicol 17, 497–537. https://doi.org/10.1080/08958370591001121.
[38] Innes, E., Yiu, H.H.P., McLean, P., Brown, W., Boyles, M., 2021. Simulated biological fluids–a systematic review of their biological relevance and use in relation to inhalation toxicology of particles and fibres. Crit Rev Toxicol 51, 217–248. https://doi.org/10.1080/10408444.2021.1903386.
[39] Hesterberg, T.W., Hart, G.A., 2001. Synthetic vitreous fibers: A review of toxicology research and its impact on hazard classification. Crit Rev Toxicol 31, 1–53. https://doi.org/10.1080/20014091111668.
[40] Kamp, D.W., 2009. Asbestos-induced lung diseases: an update. Transl Res 153, 143–152. https://doi.org/10.1016/j.trsl.2009.01.004.
[41] Turci, F., Tomatis, M., Lesci, I.G., Roveri, N., Fubini, B., 2011. The iron-related molecular toxicity mechanism of synthetic asbestos nanofibres: a model study for

high-aspect-ratio nanoparticles. Chem - A Eur J 17, 350–358. https://doi.org/10.1002/chem.201001893.
[42] Fubini, B., Mollo, L., 1995. Role of iron in the reactivity of mineral fibers. Toxicol Lett 82/83 (951–960. https://doi.org/10.1016/0378-4274(95)03531-1.
[43] Mossman, B.T., 2018. Mechanistic in vitro studies: what they have told us about carcinogenic properties of elongated mineral particles (EMPs). Toxicol Appl Pharm 361, 62–67. https://doi.org/10.1016/j.taap.2018.07.018.
[44] Urso, L., Cavallari, I., Sharova, E., Ciccarese, F., Pasello, G., Ciminale, V., 2020. Metabolic rewiring and redox alterations in malignant pleural mesothelioma. Br J Cancer 122, 52–61. https://doi.org/10.1038/s41416-019-0661-9.
[45] Martra, G., Chiardola, E., Coluccia, S., Marchese, L., Tomatis, M., Fubini, B., 1999. Reactive sites at the surface of crocidolite asbestos. Langmuir 15, 5742–5752. https://doi.org/10.1021/la9814541.
[46] Turci, F., Colonna, M., Tomatis, M., Mantegna, S., Cravotto, G., Gulino, G., Aldieri, E., Ghigo, D., Fubini, B., 2012. Surface reactivity and cell responses to chrysotile asbestos nanofibers. Chem Res Toxicol 25, 884–894. https://doi.org/10.1021/tx2005019.
[47] Prescher, C., McCammon, C., Dubrovinsky, L., 2012. MossA: A program for analyzing energy-domain Mössbauer spectra from conventional and synchrotron sources. J Appl Crystallogr 45, 329–331. https://doi.org/10.1107/S0021889812004979.
[48] Brunauer, S., Emmett, P.H., Teller, E., 1938. Adsorption of Gases in Multimolecular Layers. J Am Chem Soc 60, 309–319. https://doi.org/10.1021/ja01269a023.
[49] Fantauzzi, M., Rossi, G., Elsener, B., Loi, G., Atzei, D., Rossi, A., 2009. An XPS analytical approach for elucidating the microbially mediated enargite oxidative dissolution. Anal Bioanal Chem 393, 1931–1941. https://doi.org/10.1007/s00216-009-2613-3.
[50] Fantauzzi, M., Pacella, A., Atzei, D., Gianfagna, A., Andreozzi, G.B., Rossi, A., 2010. Combined use of X-ray photoelectron and Mössbauer spectroscopic techniques in the analytical characterization of iron oxidation state in amphibole asbestos. Anal Bioanal Chem 396, 2889–2898. https://doi.org/10.1007/s00216-010-3576-0.
[51] Fantauzzi, M., Pacella, A., Fournier, J., Gianfagna, A., Andreozzi, G.B., Rossi, A., 2012. Surface chemistry and surface reactivity of fibrous amphiboles that are not regulated as asbestos. Anal Bioanal Chem 404, 821–833. https://doi.org/10.1007/s00216-012-6190-5.
[52] Piana, F., Fioraso, G., Irace, A., Mosca, P., D'Atri, A., Barale, L., Falletti, P., Monegato, G., Morelli, M., Tallone, S., Vigna, G.B., 2017. Geology of Piemonte region (NW Italy, Alps–Apennines interference zone). J Maps 13, 395–405. https://doi.org/10.1080/17445647.2017.1316218.
[53] G. Capponi, Carta Geologica d'Italia alla scala 1.50.000 e Note Illustrative. Foglio 213–230 (Genova), Roma, 2008.
[54] Capponi, G., Crispini, L., Federico, L., Malatesta, C., 2016. Geology of the Eastern Ligurian Alps: a review of the tectonic units. Ital J Geosci 135, 157–169. https://doi.org/10.3301/IJG.2015.06.
[55] Chiesa, S., Cortesogno, L., Forcella, F., Galli, M., Messiga, B., Pasquaré, G., Pedemonte, G.M., Piccardo, G.B., Rossi, P.M., 1975. Assetto strutturale ed interpretazione geodinamica del gruppo di Voltri, 94. Bollettino Della Società Geologica Italiana,, pp. 555–581.
[56] Piccardo, G.B., ofioliti del gruppo di Voltri, Le, 1984. Alpi Liguri: caratteri primari ed interpretazione geodinamica. Mem Della Soc Geol Ital 28, 95–114.
[57] Desmons, J., Compagnoni, R., Cortesogno, L., 1999. Alpine metamorphism of the Western Alps: II. High-P/T and related pre-greenschist metamorphism. Schweiz Mineral Und Petrogr Mitt 79, 111–134.
[58] Chiesa, S., Cortesogno, L., Forcella, F., 1977. Caratteri e distribuzione del metamorfismo alpino nel Gruppo di Voltri e nelle zone limitrofe della Liguria Occidentale con particolare riferimento al metamorfismo di Alta Pressione. Rend Della Soc Ital Di Mineral e Petrogr 33, 253–279.
[59] Barale, L., Piana, F., Tallone, S., Compagnoni, R., Avataneo, C., Botta, S., Marcelli, I., Irace, A., Mosca, P., Cossio, R., Turci, F., 2020. Geological Model for Naturally Occurring Asbestos Content Prediction in the Rock Excavation of a Long Tunnel (Gronda di Genova Project, NW Italy). Environ Eng Geosci 26, 107–112. https://doi.org/10.2113/EEG-2269.
[60] Auzende, A.L., Daniel, I., Reynard, B., Lemaire, C., Guyot, F., 2004. High-pressure behaviour of serpentine minerals: A Raman spectroscopic study. Phys Chem Min 31, 269–277. https://doi.org/10.1007/s00269-004-0384-0.
[61] Groppo, C., Rinaudo, C., Cairo, S., Gastaldi, D., Compagnoni, R., 2006. Micro-Raman spectroscopy for a quick and reliable identification of serpentine minerals from ultramafics. Eur J Mineral 18, 319–329. https://doi.org/10.1127/0935-1221/2006/0018-0319.
[62] Petriglieri, J.R., Salvioli-Mariani, E., Mantovani, L., Tribaudino, M., Lottici, P.P., Laporte-Magoni, C., Bersani, D., 2015. Micro-Raman mapping of the polymorphs of serpentine. J Raman Spectrosc 46, 953–958. https://doi.org/10.1002/jrs.4695.
[63] Rinaudo, C., Gastaldi, D., Belluso, E., 2003. Characterization of Chrysotile, Antigorite, and Lizardite by FT-Raman Spectroscopy. Can Mineral 41, 883–890. https://doi.org/10.2113/gscanmin.41.4.883.
[64] Mellini, M., Trommsdorff, V., Compagnoni, R., 1987. Antigorite polysomatism: behaviour during progressive metamorphism. Contrib Mineral Petrol 97, 147–155. https://doi.org/10.1007/BF00371235.
[65] D.S. O'Hanley, Serpentinites., 1996.
[66] Schwartz, S., Guillot, S., Reynard, B., Lafay, R., Debret, B., Nicollet, C., Lanari, P., Auzende, A.L., 2013. Pressure-temperature estimates of the lizardite/antigorite transition in high pressure serpentinites. Lithos 178, 197–210. https://doi.org/10.1016/j.lithos.2012.11.023.
[67] Di Pierro, S., Groppo, C., Compagnoni, R., Capitani, G., Mellini, M., 2019. Fe-rich antigorite: a rock-forming mineral from low-temperature/high-pressure metaophicarbonates. Eur J Mineral 31, 775–784. https://doi.org/10.1127/ejm/2019/0031-2867.
[68] Petriglieri, J.R., Laporte-Magoni, C., Salvioli-Mariani, E., Ferrando, S., Tomatis, M., Fubini, B., Turci, F., 2021. Morphological and chemical properties of fibrous antigorite from lateritic deposit of New Caledonia in view of hazard assessment. Sci Total Environ 777. https://doi.org/10.1016/j.scitotenv.2021.146185.
[69] Campopiano, A., Bruno, M.R., Olori, A., Angelosanto, F., Iannò, A., Casciardi, S., Spadafora, A., 2018. Fibrous antigorite in Mount Reventino area of central Calabria. J Mediterr Earth Sci 10, 17–25. https://doi.org/10.3304/JMES.2018.012.
[70] Keeling, J.L., Raven, M.D., Self, P.G., Eggleton, R.A., 2008. Asbestiform antigorite occurrence in South Australia. In: 9th International Congress for Applied Mineralogy, 2008. ICAM,, pp. 329–336.
[71] Cavallo, A., Rimoldi, B., 2013. Chrysotile asbestos in serpentinite quarries: a case study in Valmalenco, Central Alps, Northern Italy. Environ Sci Process Impacts 15, 1341–1350. https://doi.org/10.1039/c3em00193h.
[72] Favero-Longo, S.E., Turci, F., Fubini, B., Castelli, D., Piervittori, R., 2013. Lichen deterioration of asbestos and asbestiform minerals of serpentinite rocks in Western Alps. Int Biodeterior Biodegrad 84, 342–350. https://doi.org/10.1016/j.ibiod.2012.07.018.
[73] Groppo, C., Compagnoni, R., 2007. Ubiquitous fibrous antigorite veins from the Lanzo Ultramafic Massif, Internal Western Alps (Italy): characterisation and genetic conditions. Period Di Mineral 76, 169–181. https://doi.org/10.2451/2007PM0014.
[74] Viti, C., 2010. Serpentine minerals discrimination by thermal analysis. Am Mineral 95, 631–638. https://doi.org/10.2138/am.2010.3366.
[75] Spurny, K.R., Stöber, W., Opiela, H., Weiss, G., 1980. On the problem of milling and ultrasonic treatment of asbestos and glass fibers in biological and analytical applications. Am Ind Hyg Assoc J 41, 198–203. https://doi.org/10.1080/15298668091424609.
[76] Scognamiglio, V., Di Giuseppe, D., Gualtieri, M.L., Tomassetti, L., Gualtieri, A.F., 2021. A systematic study of the cryogenic milling of chrysotile asbestos. Appl Sci (Switz) 11. https://doi.org/10.3390/app11114826.
[77] Salamatipour, A., Mohanty, S.K., Pietrofesa, R.A., Vann, D.R., Christofidou-Solomidou, M., Willenbring, J.K., 2016. Asbestos fiber preparation methods affect fiber toxicity. Environ Sci Technol Lett 3, 270–274. https://doi.org/10.1021/acs.estlett.6b00174.
[78] Assuncao, J., Corn, M., 1975. The effects of milling on diameters and lengths of fibrous glass and chrysotile asbestos fibers. Am Ind Hyg Assoc J 36, 811–819. https://doi.org/10.1080/0002889758507347.
[79] Belluso, E., Cavallo, A., Halterman, D., 2017. Crystal habit of mineral fibres. In: Gualtieri, A.F. (Ed.), Mineral Fibres: Crystal Chemistry, Chemical Physical Properties, Biological Interaction and Toxicity. EMU Notes, European Mineralogical Union and the Mineralogical Society of Great Britain & Ireland, UK, pp. 65–109. https://doi.org/10.1180/EMU-notes.18.3.
[80] Uehara, S., 1998. TEM and XRD study of antigorite superstructures. Can Mineral 36, 1595–1605.
[81] Uehara, S., Shirozu, H., 1985. Variations in chemical composition and structural properties of antigorites., Mineralogical. Journal 12, 299–318.
[82] Capitani, G.C., Mellini, M., 2005. HRTEM evidence for 8-reversals in the m=17 antigorite polysome. Am Mineral 90, 991–999. https://doi.org/10.2138/am.2005.1634.
[83] Bruker A.X.S., Topas V6: General profile and structure analysis software for powder diffraction data, Karlsruhe, Germany., 2016.
[84] Capitani, G.C., Mellini, M., 2004. The modulated crystal structure of antigorite: The m = 17 polysome. Am Mineral 89, 147–158. https://doi.org/10.2138/am-2004-0117.
[85] Campione, M., Capitani, G.C., 2013. Subduction-zone earthquake complexity related to frictional anisotropy in antigorite. Nat Geosci 6, 847–851. https://doi.org/10.1038/ngeo1905.
[86] Rozenson, I., Bauminger, E.R., Heller-Kallai, L., 1979. Moessbauer spectra of iron in 1:1 phyllosilicates. Am Mineral 64, 893–901.
[87] Mellini, M., Fuchs, Y., Viti, C., Lemaire, C., Linairès, J., 2002. Insights into the antigorite structure from Mössbauer and FTIR spectroscopies. Eur J Mineral 14, 97–104. https://doi.org/10.1127/0935-1221/2002/0014-0097.
[88] Kunze, G., 1961. Antigorite, Fortschr Der Mineral 39, 206–324.
[89] Glusker, J.P., 1980. Citrate Conformation and Chelation: Enzymatic Implications. Acc Chem Res 13, 345–352. ⟨https://pubs.acs.org/sharingguidelines⟩.
[90] Oze, C., Solt, K., 2010. Biodurability of chrysotile and tremolite asbestos in simulated lung and gastric fluids. Am Mineral 95, 825–831. https://doi.org/10.2138/am.2010.3265.
[91] Schott, J., Berner, R.A., 1983. X-ray photoelectron studies of the mechanism of iron silicate dissolution during weathering. Geochim Cosmochim Acta 47, 2233–2240. https://doi.org/10.1016/0016-7037(83)90046-7.
[92] Hume, L.A., Rimstidt, J.D., 1992. The biodurability of chrysotile asbestos. Am Mineral 77, 1125–1128.

[93] Andreozzi, G.B., Pacella, A., Corazzari, I., Tomatis, M., Turci, F., 2017. Surface reactivity of amphibole asbestos: A comparison between crocidolite and tremolite. Sci Rep 7. https://doi.org/10.1038/s41598-017-14480-z.

[94] Freyria, F.S., Bonelli, B., Tomatis, M., Ghiazza, M., Gazzano, E., Ghigo, D., Garrone, E., Fubini, B., 2012. Hematite nanoparticles larger than 90 nm show no sign of toxicity in terms of lactate dehydrogenase release, nitric oxide generation, apoptosis, and comet assay in murine alveolar macrophages and human lung epithelial cells. Chem Res Toxicol 25, 850–861. https://doi.org/10.1021/tx2004294.

[95] Lim, H., Lee, J., Jin, S., Kim, J., Yoon, J., Hyeon, T., 2006. Highly active heterogeneous Fenton catalyst using iron oxide nanoparticles immobilized in alumina coated mesoporous silica. Chem Commun 463–465. https://doi.org/10.1039/b513517f.